

July 20, 2021

Announcements

- **Required:** Neurotechnology and Neuroscience Industry Opportunities with Dr. Scott Ransom (CNT Director of Industry Relations and Innovation) - Thursday, 7/22, 9-10 am (PST),
<https://washington.zoom.us/j/94718597817>
Meeting ID: 947 1859 7817
- **Optional:** NSF Graduate Research Fellowship Program (GRFP) webinar - Thursday, 7/22, 5-6 pm (PST),
<https://washington.zoom.us/meeting/register/tJYsc-qsqDovHN1iKIL08LZvrwIHxsqo9Lq4>
- **Optional:** US FDA Roundtable - Friday, 7/23, 10-11 am (PST): Dialog with people engaged in neurotechnology product development and academic researchers that are translating and de-risking neurotechnologies. Topics will include regulatory science gaps and tools to accelerate neurotechnology medical device innovation.
<https://washington.zoom.us/j/99936210903>
Meeting ID: 999 3621 0903
- **Optional:** National Science Foundation GRFP information session, Monday, 7/26, 10 am (PST). Registration is required at:
https://zoom.us/meeting/register/tJcqduytrT8qGNfwRI_OzG03C79Dq9Y7PGIf
- **Optional:** Be part of a student panel! Friday, August 6, ~10:30-11:30 am (PST)

Posters vs. Talks

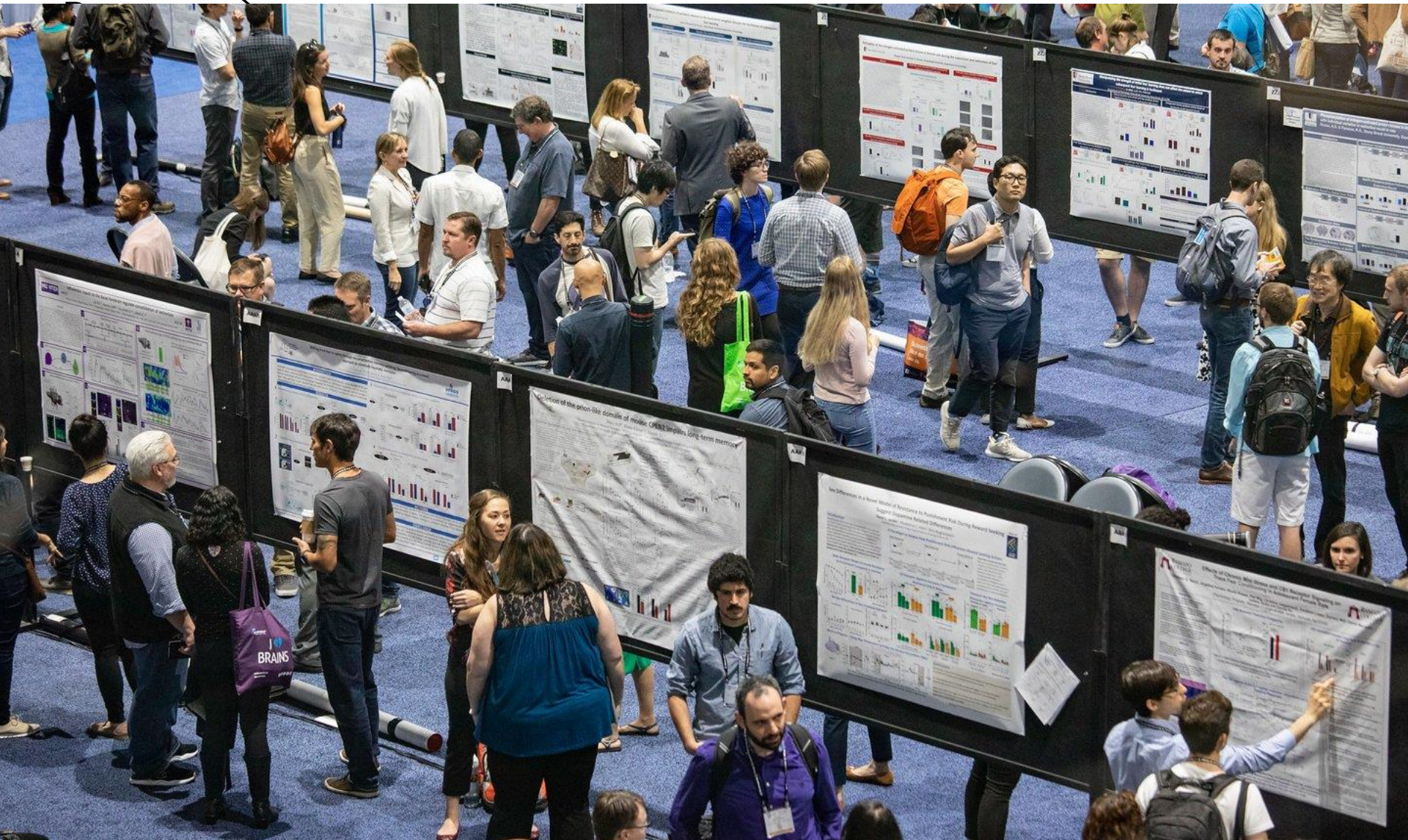
	Poster	Talk
Difficulty to Prepare		
Time to Prepare		
Audience Reached		
Stress Level		

Poster Mechanics

Your Poster = XX (height) by YY (width) (allows a margin)

Foam Board or Backing = (XX + a) by (YY + a)

Foam Board



Poster Mechanics

Background



Titles

- First (only?) thing that people
- Encourage (lure) people to your poster
- Include a question: yes or no?
- Define scope of the study
- Include a significant result or finding
- Not too long
- Like a newspaper headline

 **Title Review** 

- Share potential title with people in breakout rooms.
- Revise title?
- Share title(s) with group.

Poster Mechanics

Required Components

1. Title
2. Authors (you will be the first author; lab director likely last; mentors and others in the middle)
3. Affiliations (Departments, Universities, City, State)
4. CNT Logo
5. NSF Logo
6. Grant Acknowledgment Statement



CENTER for
NEUROTECHNOLOGY
a National Science Foundation Engineering Research Center



Poster Mechanics

Suggested Components

- 1. UW Logo**
- 2. Your Home University Logo**
- 3. Section headings**
 - A. Introduction**
 - B. Methods**
 - C. Results**
 - D. Discussion**
 - E. References**

Poster Mechanics

Hints and Tips

1. **Know your audience.**
2. **Less is usually better than more.**
3. **Simplify graphics (if possible), but use them.**
4. **Text should be readable from a distance.**
5. **Use PowerPoint, Illustrator, InDesign...**
6. **Do not justify paragraph margins.**
7. **Avoid poor resolution graphics.**
8. **Be careful with color.**
9. **Be careful with busy backgrounds.**

Poster Critique

- **Groups of students (~3 per group)**
- **Each group has three posters (see PDF).**
 - Room 1 = posters 1-3 | Room 2 = posters 4-6 | Room 3 = posters 7-9
 - Room 4 = posters 10-12 | Room 5 = posters 13-15 | Room 6 = posters 16-18
 - Room 7 = posters 19-21 | Room 8 = posters 21-24
- **Spend ~3 min/poster**
 - **Layout/organization/style**
 - **Content**
 - **Font**
 - **Color**
 - **Background?**
- **Present to group (1-2 min/poster)**

Dorsal root ganglia neural recordings with a novel non-penetrating thin-film microelectrode array

Zachariah J. Sperry^{1,2}, John P. Seymour³, Fan Wu³, Shani E. Ross^{1,2}, Kanghwan Kim³, John T. Bentley^{1,2}, Euisik Yoon³, Tim M. Bruns^{1,2}

1. Biomedical Engineering, University of Michigan, Ann Arbor
2. BioInterfaces Institute, University of Michigan, Ann Arbor
3. Electrical Engineering and Computer Sciences, University of Michigan, Ann Arbor

DRG as Neural Interface

Dorsal root ganglia (DRG) are clusters of **sensory cell bodies** just outside of the spinal cord.

Recording and decoding neural information from the DRG gives insight regarding peripheral sensory systems for investigating neurophysiology and developing neural prostheses.

Current **microelectrode** interfaces can record from **single neurons**, but the shanks must be introduced by **penetrating the epineurium**.

These arrays were designed for the cortex and are not well matched to DRG morphology.

Additionally they can **cause inflammatory response and scarring**.

Device **design should be driven by anatomical data**, both qualitative and quantitative. For example, penetrating electrode shank lengths for motor cortex are often chosen to record from layer 5 neurons.

GOAL: To design, fabricate, and evaluate a novel microelectrode array for neural recording in the DRG.

DRG Anatomy » Device Design

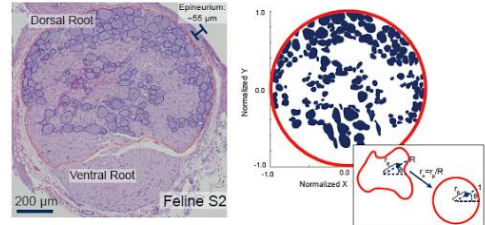
DRG anatomical observations:

- On the scale of microelectrode arrays, DRG are curved rather than flat, so array should **curve or conform to the surface**.
- DRG cells bodies are concentrated near the dorsal surface, so advantageous to **record primarily in this upper layer** (see below for quantitative analysis).
- The epithelial layer is thin enough (25-100 μm) to record through, potentially allowing a **non-penetrating dorsal surface** approach.

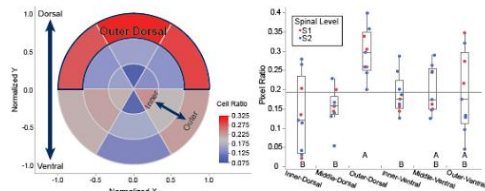
Previous studies with recording single units from the surface of neural tissue:

- Cortex (Khodagholi et al. 2014)
- DRG (Gaut & Bruns 2011). The DRG electrodes used required downward force to make good contact, but ideally an array would **require only surface tension**.

DRG cross-section showing edges (red = DRG, blue = cell body, green = nucleus) Cell bodies (blue pixels) transformed to a circular area for comparative analysis [Inset: transform method]



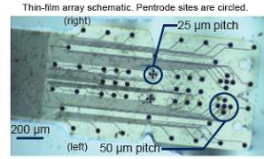
Average ratio of cellular pixels to normalized area by annular sector. Pixel ratios by annular sector. Regions that are not connected by same letter are significantly different



Novel Thin-Film Array

Array specifications:

- 64 channels
- Polyimide substrate [3.6 μm thick]
- Gold interconnects [400 nm thick]
- Iridium electrode sites
 - 1130 μm^2 & 400 μm^2
 - Impedance: 173 & 369 (± 35) k Ω
 - 4 sets of "pentodes" (5 closely spaced sites)

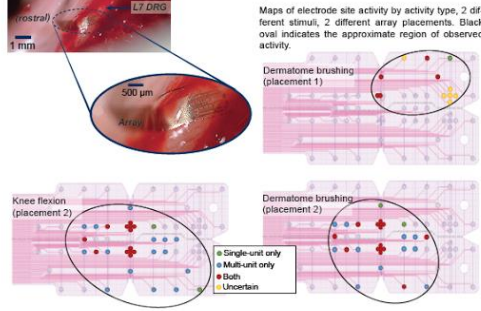


Surgery and In Vivo Recordings

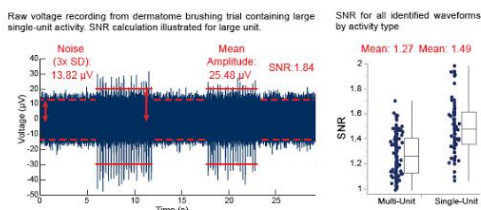
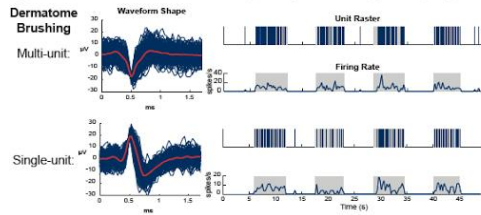
After laminectomy to expose the spinal roots, array was placed on the L7 DRG of a feline under isoflurane anesthesia. **Surface tension was used** to secure the array.

In vivo image of thin-film array on L7 DRG Recorded neural activity (30 kHz) with Ripple Grapevine system. Sorting offline.

Single- and multi-unit activity observed during cutaneous dermatome brushing and joint flexion on **35/64 unique channels**.



Single- and multi-unit waveforms for dermatome brushing trial. Gray boxes indicate (approximate) stim periods



Source Localization

In some trials, **simultaneous single-unit activity** was observed on all five sites in a **pentode** (3/4 pentode sites; both 25 μm & right 50 μm).

Assuming a **point-current source in a homogeneous medium**:

$$V = \frac{k}{\sqrt{x^2 + y^2 + z^2}} \quad k = \frac{I}{4\pi\sigma} \text{ , assumed constant}$$

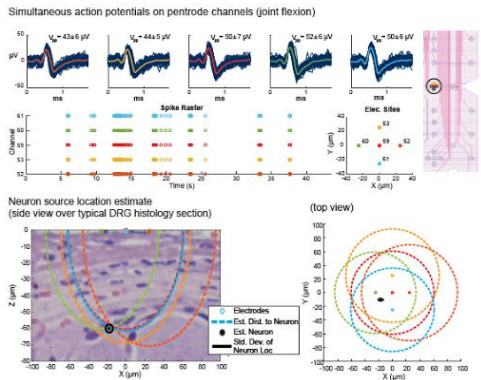
V: Voltage | x, y, z: Cartesian distances from source | I: Current | σ : Conductivity

Linear algebraic techniques for tetrode (Lee et al. 2007) estimate signal source location as the **intersection of 5 source-electrode radius estimates** from each site.

For a pentode, four estimates of location can be made.

Estimate **required site curvature estimate**. Curve radius chosen was 500 μm .

Location estimates were only possible for 25 μm pentode sites. Estimate for the 50 μm pentode did not converge to a reasonable solution.



Conclusions & Future Work

Using a conforming thin-film array, we successfully recorded from the DRG surface. We observed both single- and multi-unit activity. Waveforms on pentode sites contained spatial information used to estimate signal source, which is a novel analysis in DRG.

Going forward, we will refine the **array layout** by increasing the number of polytrode sites and shaping it for the DRG profile as supported by the NIH SPARC program. We will use source localization to **explore DRG neurophysiology** and anatomy by mapping activity with different stimuli.

Finally, we will explore **electrical stimulation and chronic array placement** toward therapeutic goals (ex. bladder neuroprostheses).

Acknowledgements

I would like to acknowledge pNEURO Lab members Kaile Bennett, Abeer Khurram, Anastasia Ostrowski, and Chris Stephan.

The array was manufactured at the Lurie Nanofabrication Facility at the University of Michigan.

Funding provided by the Craig H. Neilsen Foundation (Grant #314980) and by the University of Michigan MiBrain Initiative.

Whole genome computational analysis of tRNA-derived small RNAs in Arabidopsis thaliana RNA biogenesis mutants

Wojciech Karlowski, Agnieszka Thompson, Patrycja Plewka, Maciej Szymanski, Andrzej Zielezinski, Przemyslaw Nuc, Artur Jarmolowski

Department of Computational Biology & Department of Gene Expression, Adam Mickiewicz University in Poznan, Poland

<http://combio.pl>

ABSTRACT

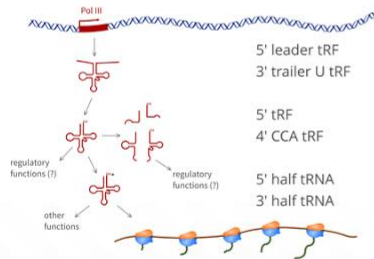
In recent years, application of the high-throughput sequencing technologies revealed a novel class of abundant, **stable, non-coding RNAs, derived from tRNA (tRFs)**. Using *Arabidopsis thaliana* as a model organism, we aim at identification and characterization of the components involved in tRNA and microRNA biogenesis pathways that may play a role in generation of tRFs.

We are presenting our results of a global characterization of small RNAs originating from *Arabidopsis* tRNA and tRNA-like genomic sequences. In addition to our own experimental data from over **20 A. thaliana strains** carrying mutations in genes associated with tRNA and microRNA biogenesis, the set includes all high quality *Arabidopsis* short RNA sequences from public sRNA-Seq databases. Thus, the entire dataset provides a broad perspective of tRNA-derived short RNAs in *Arabidopsis* for a wide cross-section of tissues, developmental stages, as well as biotic and abiotic stress conditions. An advanced and user-friendly exploration of datasets and results of the analyses were implemented in a form of the **"T-regs"** web portal.

INTRODUCTION

tRF types:

tRFs: short RNA fragments derived from tRNA



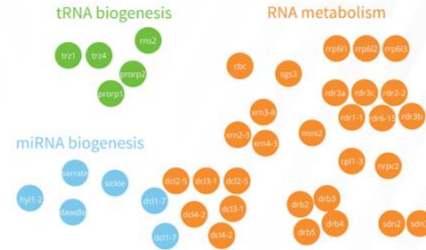
METHOD

Data processing schema (*Arabidopsis* as model organism)

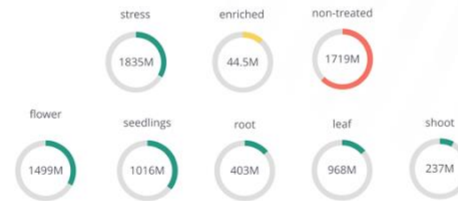


MATERIALS

RNA biogenesis mutants

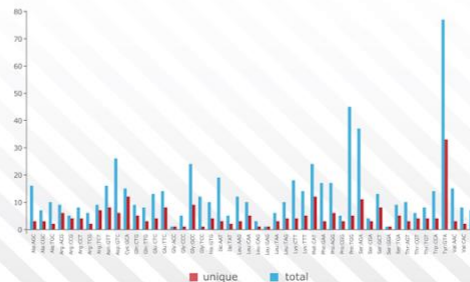


Public samples: environmental / stress



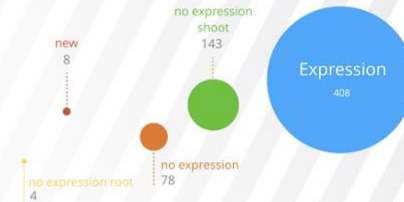
tRNA genes: GtRNAdb / TAIR 10

638 genes / 237 unique sequence variants / 48 anticodons

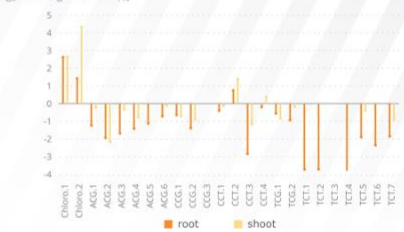


RESULTS

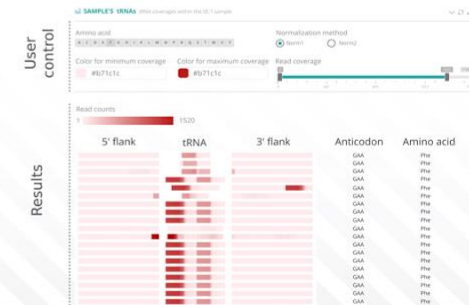
tRNA-Seq: re-annotation of tRNA
tRNA expression in shoot and root tissues



tRNA-Seq: landscape of tRNA expression
log₂(tRNA-Arg/tRNA-Met(i))



t-Regs: tRFs database



ACKNOWLEDGMENTS

This work was supported by grant from the National Science Center 2011/03/B/NZ2/01416 and the KNOW RNA Research Centre 809 in Poznan (No. 01/KNOW2/2014)

CHALLENGE

LACK OF TALENT: Videos were constrained to the limited drawing and video making abilities of the main contributors

LACK OF TIME: Videos needed to be produced on top of a busy academic workload

TO BE SUCCESSFUL, the channel needed to post regular, high quality videos that appealed to a broad audience, while providing useful information

LACK OF RESOURCES: Limited equipment was available

EVIDENCE-INFORMED DECISIONS on human health require at least a rudimentary understanding of the science underlying potential risks

MEMBERS OF THE PUBLIC and others want more accessible, understandable and credible information on health risks

OVER 1 BILLION UNIQUE USERS visit YouTube each month worldwide, watching over 6 billion hours of video per month

SCIENCE EDUCATION CHANNELS like SciShow and Minute Physics have upward of 2 million subscribers

RISK BITES WAS CREATED in response to an opportunity to use YouTube in a unique and powerful way to help people understand the basic principles of evidence-informed approaches to understanding and addressing risk

An integrated strategy of dissemination using social media and networks is used to raise awareness

VIEWING TIME: Viewers currently spend approximately 450 hours per month watching RiskBites videos - the equivalent of 19 days per month

VIEWS: Risk Bites videos currently receives around 13,000 views per month

CLOSED CAPTIONS: All videos have English subtitles for the hearing-impaired

GEEK OUT ON THE SCIENCE OF RISK

Providing accessible educational resources on risk science using **YouTube**

IMPACT

QUALITATIVE INDICATORS OF SUCCESS: More qualitative indicators of success include word of mouth from users, link sharing, and the degree to which professional organizations actively use and share the videos

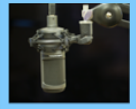
Story Board



Script



Narration & Backing



Video



Closed Captions



Final Video



PROCESS

Analysis of a mutant mouse model lacking histone3-lysine27 N-methyltransferase EZH2 in developing lung epithelium

ABSTRACT

Histone modification is important for epigenetic regulation of gene expression. Histone3-lysine27 N-methyltransferase EZH2 is part of a protein group called the polycomb repressive complex-2 (PRC2) and primarily plays a role in gene silencing by adding three methyl groups to H3K27, causing chromatin to condense and silencing the genes encoded in the condensed DNA. The role of EZH2 as to which genes are silenced and which are expressed in the developing lung is not clear. Using homologous recombination, mice were genetically engineered such that the promoter for signaling pathway gene *Sonic hedgehog* (*Shh*) drives the expression of Cre recombinase. Since developing lung epithelium cells express *Shh*, the expression of Cre recombinase combined with the insertion of *LoxP* sites in the introns of *Ezh2* led to the removal of EZH2 from developing lung epithelium in this knock-out model. We report successful confirmation of the absence of the EZH2 protein in the lung epithelium at different embryonic developmental stages by genotyping with PCR and analyzing phenotypes by fluorescent immunohistochemistry. Mice homozygous for the removed *Ezh2* alleles had phenotypically abnormal lung development during late gestation. Consequently, this mouse model may allow for further study of the role of EZH2 in lung development and its effects on gene expression.

INTRODUCTION

DNA is packaged around histones in the cell nucleus, and the way the DNA is packaged is important for gene expression. Histone expression is dynamic and can be changed by methylation of lysine residue of the histones. Methylation of H3K27 has been shown to be affiliated with gene silencing. EZH2 is important for maintaining cell fate and differentiation by silencing genes during development and is the main methyltransferase for H3K27. Mutations in EZH2 result in developmental problems such as Weaver syndrome.

METHODS

In one mouse line, bacterial *LoxP* sites were inserted into the introns of *Ezh2* flanking the *Ezh2* exons. For another mouse line, the promoter of *Shh* drives the expression of Cre recombinase. These two lines were then bred together to create the mutant mice, which is both *Ezh2^{fl/fl}* and *Shh-cre^{+/+}*. Mutant mice die at birth. Lungs that lack *Ezh2* in the epithelium have smaller alveolar sacs and a thicker mesenchyme.



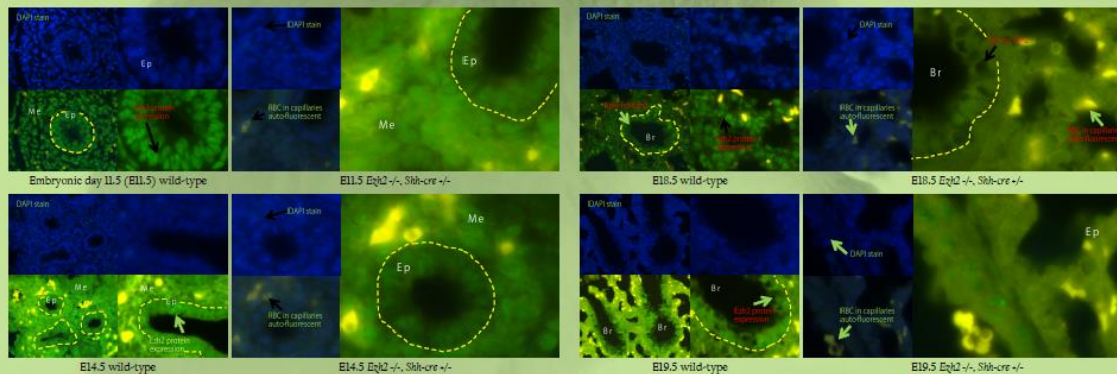
MUTANT MOUSE MODEL

- Cre recombinase is expressed where *Shh* is expressed during development
- Thus, Cre recombinase removes the *Ezh2* gene in lung epithelia
- Genotyping using PCR to detect alleles
- Absence of *Ezh2* was confirmed through fluorescent immunohistochemistry using an antibody against *Ezh2*

RESULTS

FLUORESCENT IMMUNOHISTOCHEMISTRY

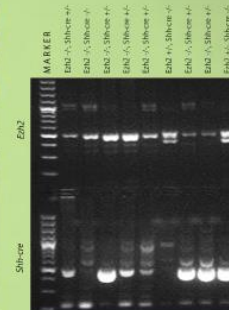
Different developmental time points were evaluated using an antibody against *Ezh2*. Slides were also stained with DAPI to visualize the nuclei, and the two images were overlaid to see where staining for *Ezh2* showed.



Br = bronchiole, Ep = epithelium, Me = mesenchyme, RBC = red blood cell

PCR

To genotype the mice, PCR was used to detect individual alleles. Samples were run on a 2% agarose gel during gel electrophoresis.



CONCLUSION

In mutant mice, the majority of the *Ezh2* protein was knocked out in the lung epithelium. The presence of *Ezh2* in some of the lung epithelia indicates that Cre recombinase was not complete. The incomplete knockout of *Ezh2* depends on the half-life of Cre recombinase and its expression; if Cre activity is not strong enough, *Ezh2* may not be knocked out in that cell, leading to signal during immunohistochemistry.

Next step: to stain for the expression of activated Cre recombinase and to compare its expression pattern to that of *Ezh2* in the mutant mice.

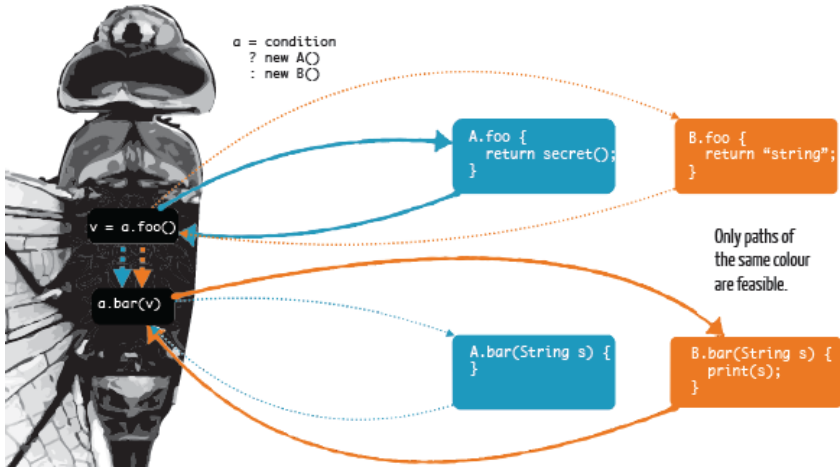
REFERENCES

- Crowley, M. L., MacQuibban, K. L., Peng, A. F., Yao, Z., and Tapscott, D. J. (2003). Polycomb-mediated repression during terminal differentiation: what don't you want to be when you grow up. *Gene and Development* 17, 697-705.
- Harigita, M. and Moriyama, E. (2004). Lung development: re-examining the generation and regression of a complex organ. *Development* 131, 503-513.
- Langstaffe, T. A., Isaacson, L., Harikrishnan, P., Chinnaiyan, C., Cao, Y., Chen, J. C., Blevins, L. W., Miao, H., Rodriguez, J., Chen, S. S., Dorekas, A., Serra, M., White, D. J., Gonsky, R., Chinnaiyan, P., Wang, S., Krasna, M. J., and Roberts, D. W. (2010). Enhanced formation of Purified Lung and Thymus Progression from Fibroblasts. *Stem Cells* 28(10), 186-191.
- Millon, C., Boudreau, L., Gauthier, M., Chen, P. N., Li, J., Eppe, A., and Ramirez, M. J. (2006). Characterization of the mid-range oncogene identifies genes regulated during lung bud initiation. *Gene Expression Patterns* 6, 126-136.
- Montell, C., Carballo, W., Lopez, R. E., Sakonchik, M., Akman, S. H., Al, K., Albertson, K. C., Blank, B. D., Chapman, H. A., Checkley, W., Epstein, J. A., Kimmey, C. G., Lomen, M., Murren, P., Nakano, T. J., Mikkelsen, D. E., Mikkelsen, T. E., Petrij, S. J., Petrij, J., Ramirez, J., Blk, W., Shen, Z., Wang, Z., Williams, J. A., Gu, D., Blankenhorn, C. J., and Gu, Q. X. (2012). Molecular Development of Lung Development. *Annals of the New York Academy of Sciences* 1262, 20-26.
- O'Connell, D., Williams, M., Pagan, M., Nopich, K. C., Trowel, M. A., and Greenwell, T. (2001). The Polycomb complex (PcG) is required for B-lymphocyte development. *Molecular Cellular Biology* 21, 4110-4116.
- Spemann, A., and Nieuwkoop, M. (1938). Polycomb chromatin control cell fate, development and cancer. *Nature Reviews Cancer* 6, 941-952.

5

DATA FLOW ANALYSIS IN THE PRESENCE OF CORRELATED CALLS

Marianna Rapoport, Ondřej Lhoták, Frank Tip
University of Waterloo



summary
THE PRECISION OF DATA-FLOW ANALYSES CAN BE IMPROVED IN THE PRESENCE OF CORRELATED CALLS.

intro
IS YOUR DATA REALLY SECRET?
Data-flow analysis (DFA) approximates properties of programs without running them. For instance, in a **taint analysis**, we find out which variables are **secret**, e.g. to discover confidential information leaks. However, **infeasible paths** in a program's control-flow graph can affect the accuracy of an analysis.

goal
ELIMINATE INFEASIBLE PATHS
An infeasible path is one that cannot occur during program execution. In an object-oriented language, two method calls are **correlated** if they dispatch to multiple targets. The goal of this work is to **eliminate** the infeasible paths caused by correlated calls.

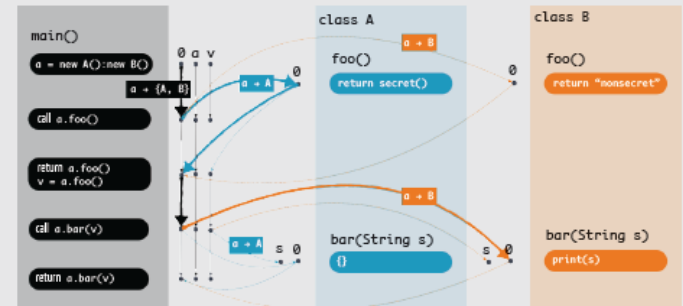
result
CORRELATED CALLS ANALYSIS
The correlated calls analysis improves the precision of IFDS results that contain correlated calls. Infeasible paths caused by correlated calls are removed by transforming an IFDS problem into a special type of IDE problem and solving the latter.

problem
IMPROVING THE PRECISION OF IFDS
We focus on the DFA problems that can be solved with the IFDS* (Reps et al., 1995) algorithm. IFDS works by converting a DFA problem to a graph reachability problem on an **exploded supergraph** (see figure →). However, it can only solve binary decision problems (e.g. “is a variable secret?”), and is not powerful enough to keep track of correlated calls.

* Inter-procedural Finite Distributive Subset problem

method
A TRANSFORMATION FROM IFDS TO IDE
The IDE** (Reps et al., 1996) algorithm can solve a larger set of problems than IFDS. IDE encodes a DFA problem with a **labeled exploded supergraph**. The graph edges are labeled with **flow functions**. We convert an IFDS problem to an IDE problem that uses flow functions to keep track of correlated calls. The flow functions serve to “remember” the enclosing classes of dispatched methods.

** Inter-procedural Distributive Environment problem



FIND OUT MORE

- How do IFDS and IDE work?
- How are flow functions represented?
- How can we implement the correlated-calls analysis?
- How do we know the analysis is correct?

cs.uwaterloo.ca/~mrapopor

Inside a Feather

Laminar Layup Varies Around and Along Bird Feather Shafts

Since feathered flight developed more than 150 million years ago, the central shaft of a bird feather has evolved under selection pressures to become light, stiff, and strong. As a result, the shaft has become a complex, fibre-reinforced biocomposite beam.

In quantifying the mechanical properties of feather shafts, previous researchers have reported values of flexural rigidity which vary over two orders of magnitude. Some of this variation can be explained by changes in geometry. However, the laminar layup of the shaft, cortex and the micromechanics of these laminae have not yet been considered.

We have previously shown that the number of laminae varies between species of birds, and that these laminae are anisotropic (Laurent et al. 2014). This variation means that it is necessary to understand not only the geometry of feather shafts, but also their laminar layup and the micromechanics of those laminae before we can understand and predict the macromechanical behaviour of the feather shaft.

Here, we present data gathered at different locations on a feather shaft (rachis and calamus) using Synchrotron Radiation Computed Tomography (SR-CT). This gives us a detailed insight into the laminar layup and the orientation of the internal fibres. This is the first step in understanding the mechanical properties of feather shafts from the inside.

Method

The Swiss Light Source (SLS), at the Paul Scherrer Institute (Switzerland), is a third-generation synchrotron light source. It provides a high-brightness photon beam which enables CT scanning at resolutions three orders of magnitude higher than a typical hospital-based scanner, with scan times as short as six minutes. With these scans, we capture the three-dimensional void orientation in rachis material. Using transmission electron microscopy, these voids were found to be aligned with the internal fibres.

Samples ($L = 5$ mm) were removed from the leading flight feather of a Whooper Swan (*Cygnus cygnus*) at 10, 30, 50, 70, and 90% of the shaft length and scanned. Overlapping regions of interest were stitched together and the whole sample was reconstructed with voxel dimensions of 325 nm. The largest sample (10%) required 42 individual scans and the smallest (90%) only six. Scans were stitched together using a Fourier-shift algorithm where possible, or with the Mosaic tool in ImageJ/Fiji.

Results & Conclusion

Our SR-CT scans reveal geometry of the shaft changing along the length of the feather. Looking more closely they show how the number, orientation, and thickness of laminae vary within the shaft. Therefore, our results show that laminar layup varies around, and along, a bird feather shaft.

These variations in geometry and laminae influences the rachis mechanics. Next, to fully understand the implication for the feather mechanics, we will determine the modulus of individual laminae.

Flight feathers are light, strong and stiff and allow heavy birds, such as a whooper swan, *Cygnus cygnus*, to fly.

Each flight feather has a shaft, which changes in geometry along its length, like the second flight feather (pictured).

Ultra high resolution Computed Tomography reveals that the number and thickness of differently oriented laminae varies around and along the feather shaft.

bioRxiv preprint doi: <https://doi.org/10.1101/009691>; this version posted October 22, 2014. The copyright holder for this preprint (which was not certified by peer review) is the author/funder, who has granted bioRxiv a license to display the preprint in perpetuity. It is made available under aCC-BY-NC-ND 4.0 International license.

LAURENT, CM¹, SCHNEIDER, P¹, DIXE, G², BOARDMAN, RP¹, PALMER, C³, COOK, RB⁴, DE KAT, R¹,
¹Aerodynamics and Flight Mechanics, Engineering and the Environment, University of Southampton, UK
²Ocean and Earth Science, National Oceanography Centre Southampton, UK
³Avionics, Engineering and the Environment, University of Southampton, UK
⁴Department of Evolutionary Biology and Systematics, University of Debrecen, Hungary
⁵Centre for Computed Tomography, University of Southampton, UK
⁶Carl's national Centre for Advanced Biology, Engineering and the Environment, University of Southampton, UK

Cloning, expression and characterization of GH10 xylanases from landfill leachate bacteria *Paenibacillus* sp. MAEPY2

Patric Chua^{1*}, Gary A Dykes², Lee Sui Mae¹

¹School of Science, Monash University, Malaysia

²School of Public Health, Curtin University, Australia

*Corresponding author e-mail: tchua4@student.monash.edu

Background

- Landfill wastes are usually materials with plant biomass, e.g. food/organic wastes, papers and horticultural wastes.
- Major components in plant biomass can be degraded rapidly (in a few days) by soil microbes in landfills.
- Plant biomass-degrading microbes can be exploited for applications in various industrial processes.

Bioprospecting

Landfill leachate was collected from a local landfill site.



Figure 1: Leachate treatment pond at Jemur Saniary Landfill, Selangor, Malaysia.



Microbial population in leachate was cultured on minimal media containing cellulose.



Figure 2: *Paenibacillus* sp. MAEPY1 and MAEPY2 under Orange Red stain showing cellulolytic ability.

Isolates that were capable of degrading cellulose was isolated and identified as *Paenibacillus* sp. MAEPY1 and MAEPY2.

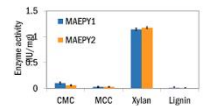


Figure 3: Enzyme activity (IU/mg) of *Paenibacillus* sp. MAEPY1 and MAEPY2 crude extracts against carboxymethyl cellulose (CMC), microcrystalline cellulose (MCC), xylan, and lignin.

Enzyme activity of both isolates further tested against substrates of other plant cell wall components. Activity against xylan was the highest in comparison.



Figure 4: Comparison of xylanase activity of *Paenibacillus* sp. MAEPY2 against commercial products at 55°C, pH 6. Crude extract of *P. sp. MAEPY2* was used as representative.

Xylanase activity of crude enzyme extract was benchmarked against commercial enzymes. Results indicate great potential.

Read more:

Chua PTC, Ho HS, Dykes G, Lee SM. 2015. Isolation and characterization of cellulose degrading ability in *Paenibacillus* isolates from landfill leachate. *Malaysian Journal of Microbiology* 11: 185-194.



Sequencing

Whole genome of *Paenibacillus* sp. MAEPY2 was sequenced using the Illumina Miseq system. Draft genome sequence was registered in NCBI GenBank under the accession no. AWUK00000000.



39% of the open reading frames (ORFs) have not been assigned any functions.



71% of the ORFs are associated with carbohydrate metabolism.



Only 3% of the 585 ORFs are putative xylanases and xylosidases.

Gene annotation of *P. sp. MAEPY2* genome was performed in the Rapid Annotations using Subsystems Technology (RAST) server¹¹. Two putative GH10 xylanase genes were identified using the EXPASY tools¹² and BLAST (P).



- Glycosyl hydrolase family 10
- Length: 963 bp, 35.3 kDa
- Has signal peptide sequence
- Expressed as extracellular protein
- Predicted isoelectric point at 8.92



- Glycosyl hydrolase family 10
- Length: 1023 bp, 39.6 kDa
- No signal peptide sequence
- Expressed as a cytoplasmic protein
- Predicted isoelectric point at 5.10

Cloning and expression

Xyn4 and Xyn5 genes were cloned into pRSET-A with 6X His-tag and transformed into *E. coli* BL21 (DE3). Expression in host cells was induced using 1mM IPTG and overnight incubation at 30°C.



Purification was performed for the His-tagged Xyn4 and Xyn5 using AKTA Purifier fast protein liquid chromatography (FPLC).



SDS-PAGE was performed following Laemmli's method¹³. A native-PAGE was performed for xylan zymography.

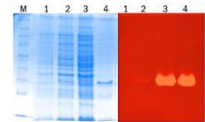


Figure 6: SDS-PAGE and zymogram analysis of the purified xylanases. Lane M: protein marker; 1-4: uninduced, induced, cell lysate, purified sample.

Enzyme studies

Optimum temperature and pH were determined via xylanase activity assay. Thermal stability was determined by pre-incubating the enzyme at various temperatures without substrates, prior to assay.

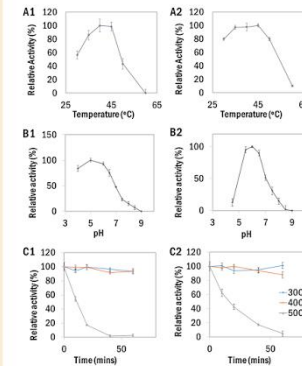


Figure 5: Effects of temperature and pH on enzyme activities of purified (A) Xyn4 and (B) Xyn5. (A) Enzyme activity was assayed at pH 7.4 and temperatures from 20°C to 60°C. (B) Enzyme activity was assayed at 40°C in 50 mM buffer systems. pH shows are represented by measured values after assay. (C) Temperature stability of the enzymes was determined at 30°C, 40°C, and 50°C, for 10, 20, 40 and 60 minutes.

In this study

We characterized two xylanase genes from *Paenibacillus* sp. MAEPY2.

Both xylanases are active from 30°C to 50°C, but work best at 40°C. Xyn4 is active at pH 4 to 7, while Xyn5 is active at pH 5 to 7.

NEXT STEPS:
A more detailed analysis of the enzyme-substrate specificity, i.e. hydrolysis products from xylooligosaccharides.

Please take one Leave your comments here Leave your contacts here

Please take one Leave your comments here Leave your contacts here

Acknowledgements

Funding for this study was provided by the Monash University Malaysia Tropical Medicine and Biology/Multidisciplinary Platform. Commercial enzymes were graciously provided by Novozymes. We are grateful to Worldwide Landfills Sdn. Bhd. for their assistance in procuring the samples, and to Malaysian Genome Institute for providing technical advice.

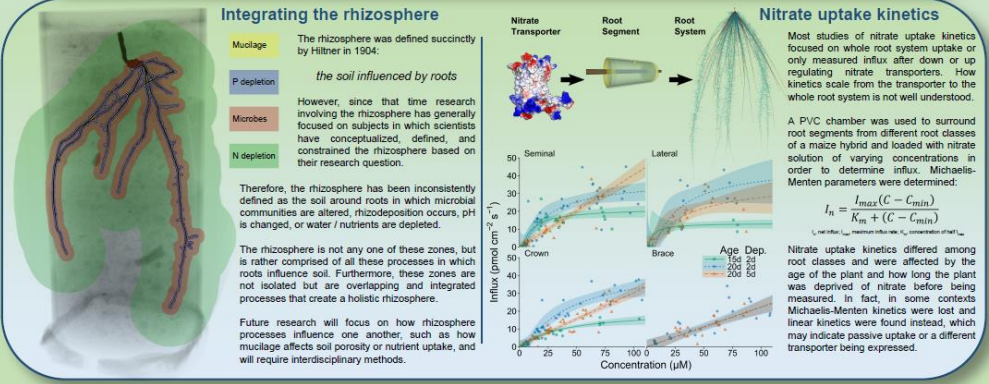
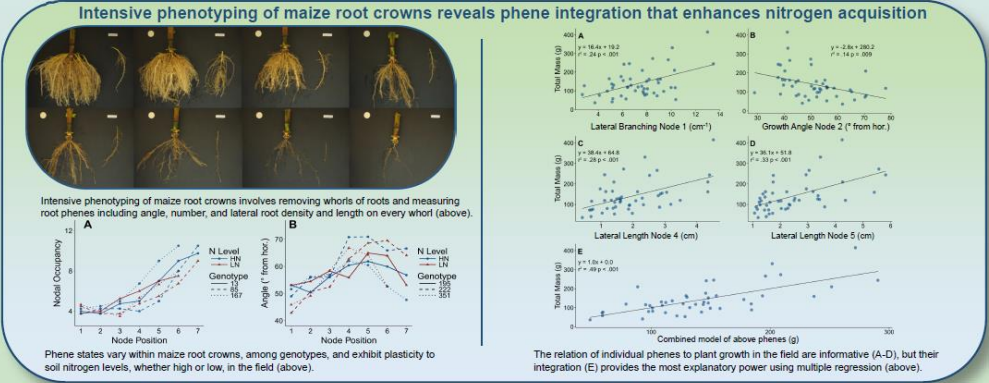
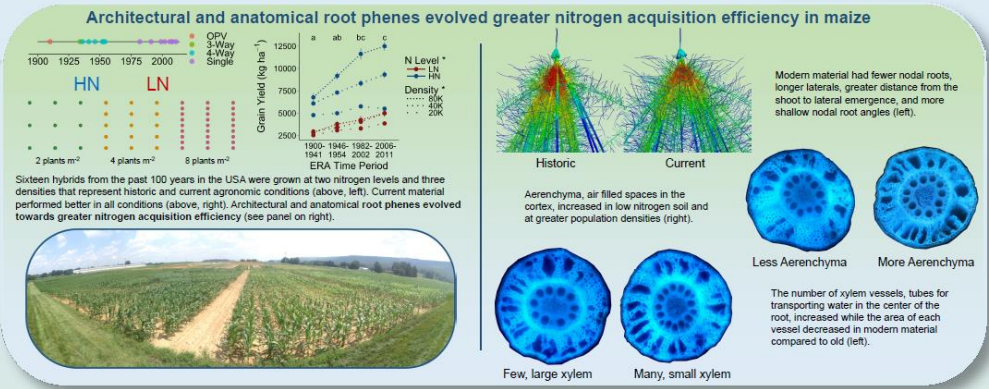
References

- Aizic et al. 2008. *BMC Genomics* 9: 75.
- Gasteiger et al. 2003. *Nucleic Acids Res* 31: 3784-3788.
- Laemmli, UK. 1970. *Nature* 227: 680-685.

Integrative root biology: scaling across transporters, the rhizosphere, the root system, and the field



Larry M. York, Jonathan P. Lynch, John Foulkes, and Malcolm J. Bennett Centre for Plant Integrative Biology University of Nottingham, UK



Topological signature in the NEXT high pressure xenon TPC

Paola Ferrario, Instituto de Física Corpuscular (Universitat de València-CSIC)

on behalf of the NEXT Collaboration



1 THE NEXT EXPERIMENT

NEXT is an experiment looking for neutrinoless double beta decay in a high pressure xenon TPC. It is located at the Canfranc Underground Laboratory (LSC), in the Spanish Pyrenees. It uses electroluminescence (EL) for energy measurement and tracking and has proven an excellent energy resolution ($\sim 0.74\%$ FWHM extrapolated to the $Q_{\beta\beta}$ of ^{136}Xe , i.e. ~ 1.98 MeV) and topological signature for background rejection in prototypes. A first stage, NEW, with ~ 10 kg of xenon, is being commissioned at the LSC — see poster P4_066 for more details.

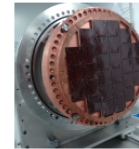
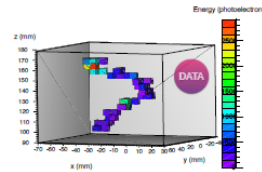
2 BACKGROUND IN NEXT

The main background in NEXT comes from high energy gammas from environmental radioactivity entering the active volume of the detector. When gammas interact with xenon gas, they can produce photoelectric and Compton electrons, at energies very similar to $Q_{\beta\beta}$. Electrons and muons coming from outside can be efficiently vetoed with fiducial cuts. See poster P4_065 for more details.

@next

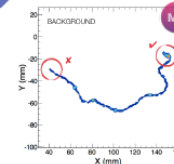
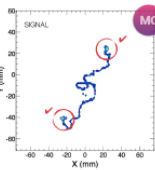
3 TRACK RECONSTRUCTION

The current track reconstruction is based on the analysis of the charge detected in each time bin by an array of silicon photomultipliers placed behind the EL area. A search for $\pm D$ hits and a subsequent voxelization of the whole space is performed, and a Breadth First Search (BFS) algorithm is used to connect the voxels to form tracks. The algorithm sorts the voxels into tracks with a criterion of connectivity, which considers two voxels as connected if their centres are closer than a maximum distance. The algorithm also finds the end-points of a track at the voxels with maximum distance along the track.



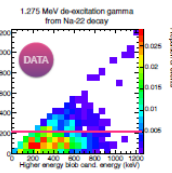
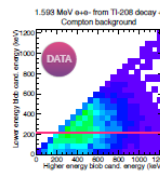
4 THE TOPOLOGICAL SIGNATURE

Electrons moving through xenon gas lose energy at an approximately fixed rate until they become non-relativistic. At the end of the trajectory they produce an energy 'blob', i.e. high energy deposition in a small region. This feature can be used to distinguish background single-electrons (one 'blob' only) from signal double-electrons (two 'blobs').



5 PROOF IN NEXT-DEMO

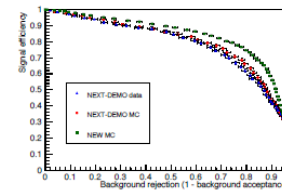
NEXT-DEMO was a 1-kg prototype, built and operated at IFIC, Valencia. We have demonstrated the power of topological cut using radioactive sources: Na-22 provides high energy electrons and Th-228 electron-positron pair production, to mimic background and signal respectively. A minimum threshold was imposed on the energy deposited at both ends of one track to pass the filter. A signal efficiency of $66.7\% \pm 0.9\%$ and a background acceptance of $24.3\% \pm 1.3\%$ is found, in good agreement with MC simulations.



JHEP 1601 (2016) 104

6 EXPECTED PERFORMANCE IN NEW

NEW will be used for background and two-neutrino double beta decay measurements, as well as to prove energy resolution and the power of topological rejection at energies close to $Q_{\beta\beta}$. Simulations indicate a significant improvement of the topological rejection, due to the larger volume of the detector. First MC studies point to $66.9\% \pm 0.6\%$ signal efficiency for $12.9\% \pm 0.6\%$ background acceptance for the same analysis as in NEXT-DEMO at a pressure of 10 bar.



7 FUTURE IMPROVEMENTS

New reconstruction approaches are being investigated. The Maximum Likelihood Expectation Minimization method tries to solve the inverse problem of finding a set of energy depositions in the chamber, given the sensor's response to the EL light. Given a statistical model that describes the forward problem, it provides estimates for the model's parameters, maximizing the likelihood of the model, given any outcome. We are also exploring the power of deep neural networks, which could be used for reconstruction and classification of events as signal or background, exploiting all possible features in the image.



This work was supported by the following agencies and institutions: the European Research Council (ERC) under the Advanced Grant 339787-NEXT; the Ministerio de Economía y Competitividad of Spain under grants CONSOLIDER-Ingenio 2010 CSD2008-0037 (CUP), FIS2014-53371-C04 and the Severo Ochoa Program SEV-2014-0398.



Ankyrin G membrane partners drive the establishment and maintenance of the axon initial segment

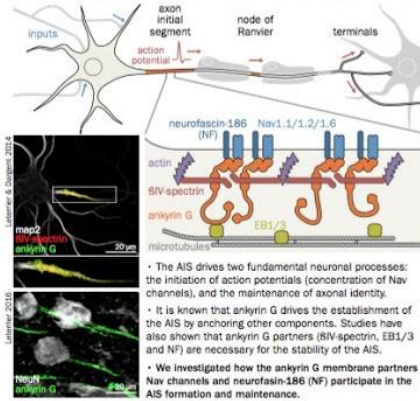
Christophe Letierrier¹, Nadine Clerc¹, Fanny Rueda Boroni¹, Audrey Montersino¹, Bénédicte Dargent¹, Francis Castets¹

1- Aix Marseille University, CNRS, CRN2M UMR 7286, Marseille, France

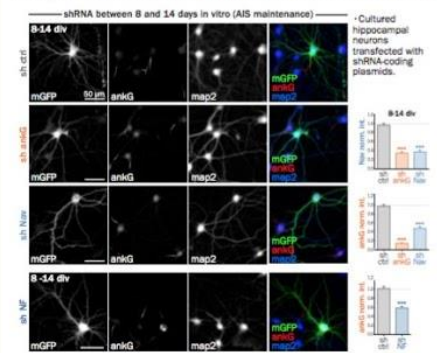
501.12 - G49



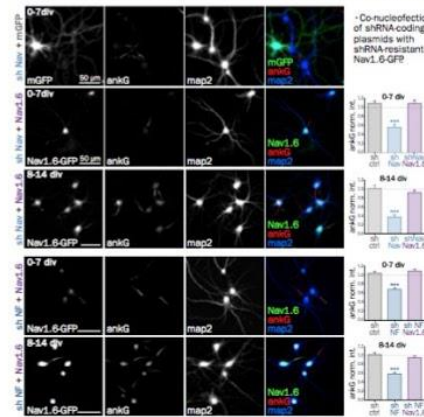
The AIS, a nexus for neuronal physiology



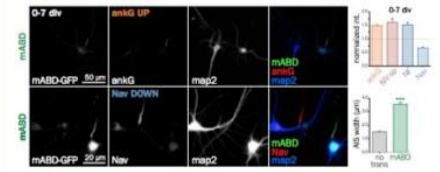
Nav/NF knockdown impairs AIS maintenance



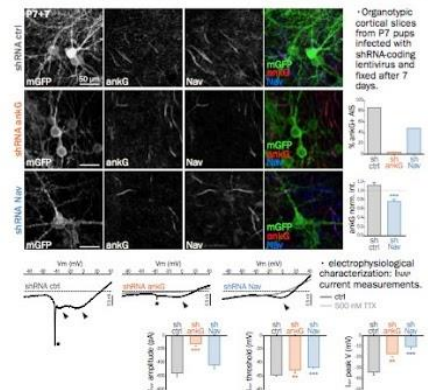
One membrane partner can rescue another



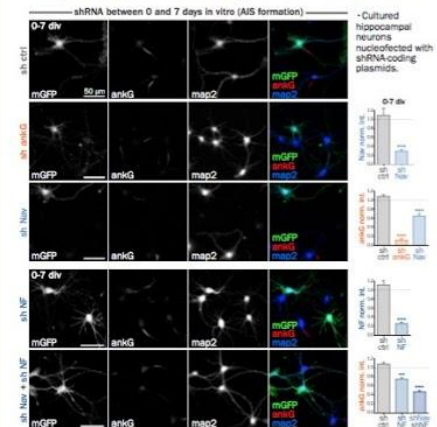
Modulation of AIS formation by mABD



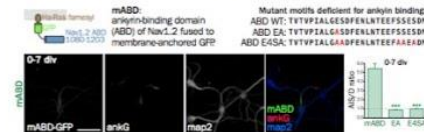
Nav channels knockdown destabilizes the AIS



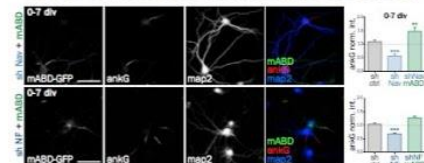
Nav/NF knockdown impairs AIS formation



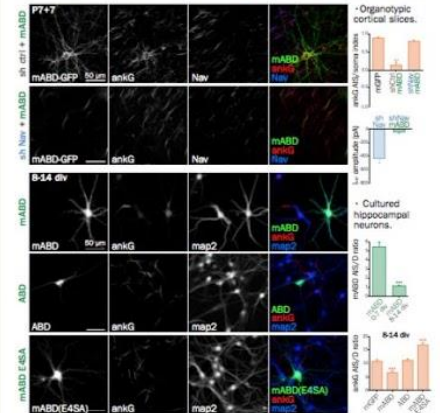
Minimal ankg membrane partner: mABD



mABD expression rescues AIS formation



mABD mislocalize ankg in mature neurons



Conclusions & perspectives

- Membrane protein partners of ankyrin G (Nav channels pore-forming subunits, neurofascin-186) contribute to both AIS formation and maintenance in cultured neurons and organotypic slices.
- They stabilize the AIS by linking ankyrin G to to the plasma membrane, as shown by the rescue obtained with a synthetic membrane-anchored ankyrin-binding domain (mABD).
- Differential effects of mABD expression during and after AIS formation suggest a slot competition mechanism with endogenous Nav channels, and a co-transport of ankyrin G and its membrane partners to the AIS.

Judge a catalyst by its anions rather than by its ligands

"Judge a man by his questions rather than by his answers." — Voltair



Luca Biasiolo

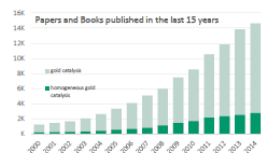
mail: luca.biasiolo@uniud.com

supervisor: Daniele Zuccaccia

Questions? Look for this guy!

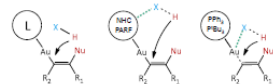
Introduction

Homogeneous gold catalysis represents a fast growing area in organic chemistry. [Chem. Rev. 2007, 107, 3180] In gold(I) catalyzed nucleophilic addition to a C=C unsaturated bond it is generally accepted that, if the rate determining step (RDS) is the nucleophilic attack, the more electron withdrawing ligands (that mean more activated substrate) will favor the reaction; whereas an inverse trend has been found when the RDS is the protodeauration. [J. Am. Chem. Soc. 2012, 134, 5697] On the other hand, also the anion plays an important role influencing the catalysis¹ but it is generally less considered. We decide to focus our effort on the rationalization of every single step of the mechanism studying this system through both experimental and theoretical approach.



3 Protodeauration

During this step the most important factors are the affinity of X⁻ with H⁺ and L-Au⁺ (that depends also on the ligand properties).⁴ The activity trends for the tested reaction show that 4 and 3 complexes follow the anion's basicity/coordination scale. While for PR₃ complexes the best anions are OTf⁻ and TFA⁻, that interacting with Au weaken the Au-C bond.⁵

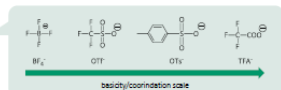
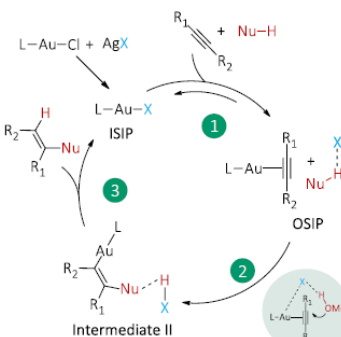
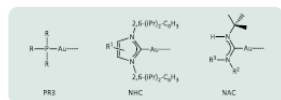


WANT MORE INFO?

Download the poster or visit us <https://aucaut.thch.unipg.it/>

AIM OF THE PROJECT

The scope of the project "Overview of gold(I) catalyzed activation of unsaturated bonds: ligands and anions effects on the cycle" is to fully study and understand all the steps that characterize gold(I) catalyzed reactions, focusing especially on the role of the ion Pairs. Notwithstanding both nature of the ligand and counterion are considered among the most important factors in gold catalysis, a rational understanding of their synergy/antagonism is still lacking.



Experimental Details

Complexes: all the gold complexes were synthesized using the proper silver salt, used in situ or isolated; those stable were achieved in high yield and characterized by NMR spectroscopy.

Ion Pairs: through a systematic NMR (¹⁹F-H HOESY) and DFT (Coulomb Potential) studies was possible to characterize all the IP.

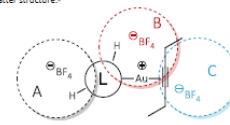
Catalysis: we tested our catalysts in two model reactions both are easily followable by NMR spectroscopy. The activity was calculated as TOF = $\frac{[\text{Product}]}{[\text{Catalyst}] \cdot \text{time}}$.

Works published during the PhD:

1. L. Biasiolo et al., Chem. Eur. J. 2014, 20, 14594.
2. G. Giancasoli et al., Organometallics 2013, 32, 4444.
3. L. Biasiolo et al., Catal. Sci. Technol. 2015, 10, 1039/0401044406
4. G. Giancasoli et al., Chem. Eur. J. 2015, 21, 2467.
5. L. Biasiolo, et al., ACS Catal. 2015, Submitted.

1 OSIP structures

With OSIP we indicate the Outer Sphere Ion Pair that is formed during the catalytic cycle. In our first work we observed that the charge (⊖) is not placed over the gold, as generally represented, but it could be delocalized all over the complex depending on the latter structure.⁷

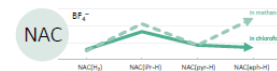


Ligands	A	B	C
1: 2-PR ₃	*	****	
2: PARF		***	**
3: NHC(Pf)	***		**
4: NHC(BIAN)	**	*	**
5: NAC(H)	****		
6: NAC(Pf-H)	***		**
7: NAC(Pf-H)	***		**
8: NAC(Pf-H)	***		**
9: NAC(Pf-H)	*	****	

1: 2-PR₃; 2: PARF; 3: NHC(Pf); 4: NHC(BIAN); 5: NAC(H); 6: NAC(Pf-H); 7: NAC(Pf-H); 8: NAC(Pf-H); 9: NAC(Pf-H).

2 Nucleophilic Attack

Nature and position of the anion are crucial when the nucleophilic attack is the RDS. We chose the alkylation of allyles, one of the oldest applications of gold(I) catalyst, as test reaction. Our experimental and theoretical experiment points out that the attack of the MeOH must be helped by the anion or by polarized additives.¹



Using the NAC series we investigated how change the IP structure functionalizing the ligand and how turn it off with the solvents.³

With the NHC and PR₃ complexes we observed how the activity is strictly related to the basicity/coordination of the anion which is, in turn, related to the ligand coordination properties.^{1,4}



CONCLUSIONS

From our results, it is evident that the correct choice of L, in order to increase the performances of gold(I) complexes, strongly depends on the nature of the anion X⁻ and vice versa.⁵ The next step will be to apply this innovative thought pattern to other gold catalyzed reactions of industrial and biological interest. In fact the possibility to use gold, instead other metals (as Hg) or Lewis acids, to activate C=C unsaturated bonds is a greener solution.

SINGLE-PEDICLED FASCIOCUTANEOUS FLAP SURVIVAL IN AGED RAT MODEL OF CHRONIC ALCOHOLISM

Edita Aksamitiene, Ph.D.^{1,2}, Sudeep Roy, M.D.¹, Kealan Hobelmann, B.S.¹, Julianna Rodin B.A.¹, Giuseppe V. Staltari, B.S.¹, Edmund A. Pribitkin M.D.¹ and Joannes B. Hoek, Ph.D.²,

PROGRAM NO: 889.13
ABSTRACT NO: 8562

¹ Department of Otolaryngology - Head & Neck Surgery, Thomas Jefferson University, Philadelphia, Pennsylvania 19107
² Department of Pathology, Anatomy & Cell Biology, Thomas Jefferson University, Philadelphia, Pennsylvania 19107

INTRODUCTION

The use of pedicled skin flaps has significantly improved the safety and functional outcomes of surgery aimed at restoring function, form and integrity of craniofacial organs after traumatic injuries or resection of tumor [1]. Single-pedicled rotational flap remains attached to the donor site via an intact vascular pedicle, which serves as a conduit for supplying nutrients and removing wastes from the flap during healing process.

Wound healing occurs through several overlapping but distinct stages: 1) hemostasis; 2) inflammation; 3) proliferation and 4) maturation. The 3rd stage occurs between 3-14 days after an injury, when the wound is 'rebuilt' with new granulation tissue. Different cell types migrate, proliferate and differentiate over an injured dermis. Many of them release angiogenic growth factors, such as VEGF, that trigger generation of new capillary blood vessels from the pre-existing vasculature to provide nutrients and oxygen to active cells with greatly increased metabolic demands [2, 3].

Various systemic factors, such as patient's old age, obesity, chronic diseases, smoking, stress etc., can prolong inflammatory phase of wound healing and impair angiogenesis [4]. Inadequate blood supply to the primary intrinsic factor affecting ischemic flap survival. In addition, under chronic hypoxic and inflammatory conditions, excessive ROS production, persistent presence of TGF β and pro-inflammatory cytokines, such as IL-6, IL-1 β and TNF α , result in enhanced synthesis and proteolytic activity of matrix metalloproteinases (MMPs) [5, 6]. Highly degradative environment, which obscures formation of granulation tissue, fibroblast proliferation and collagen production, compromises cutaneous tissue repair and predisposes to a flap to ischemic necrosis. Skin flap failure remains a significant clinical problem in surgery, which should be overcome by understanding the molecular mechanisms underlying successful flap integration [7].

GOAL OF STUDY

Both acute and chronic ethanol intake increases ROS generation [8], but it may differently modulate immune cell activation and cytokine production that in turn may improve or delay wound healing [9-11]. Here we aimed to determine if there is a statistically significant correlation between chronic alcohol-induced changes at the cellular and molecular level in aged skin and a fate of single-pedicled composite (fasciocutaneous) flap.

EXPERIMENTAL MODEL OF ISCHEMIC FLAP

Impact of chronic alcohol intake on composite flap survival and underlying signaling events was examined in isocolor pair-fed >1 year old Sprague-Dawley rats that consumed Lieber-DeCarli 32 liquid 1000 kcal/d diet consisting of 15.1% protein, 35.9% fat and either 49% carbohydrates (control group) or 13.5% carbohydrates and 35.5% ethanol (alcoholic group). Ten pairs of rats that were fed such diet for at least one year underwent surgery, where a 3.8 cm width to length ratio pedicled fasciocutaneous flap based on the inferior epigastric artery was raised in each anaesthetized rat and then rotated 90 degrees into a "defect" site that was created in the ventral surface (Fig. 1A-C). Whole pieces of skin excised from a defect site on day 0 were used as control for protein basal levels (W).

In addition, four sterile poly(vinyl alcohol) (PVA) sponges were placed in different locations under the laid flap. On post-operative day (POD) 5 (end-point) the remaining sutures were removed, an entire flap was harvested, the PVA sponges were excised and placed in the lysis buffer containing protease and phosphatase inhibitors. The animal was subsequently euthanized in CO₂ chamber. Each flap was photographed under standardized conditions, separated into proximal (P), middle (M) and distal (D) thirds (segments) (Fig. 1D), and snap frozen. For protein analysis, the flap segments were individually crushed into the powder under liquid nitrogen, and then homogenized using Potter-Elvehjem Grinding Chambers in a modified RIPA tissue lysis buffer (see Box). Protein expression was analyzed by comparative Multi-strip Western blotting (MSWB) in LD5-PAGE system [12].

- | | | |
|---|---|---|
| <ul style="list-style-type: none"> ◊ 50 mM HEPES (pH 7.4) ◊ 150 mM NaCl v ◊ 1% Triton X-100 ◊ 1 mM EGTA ◊ 10% Glycerol | <ul style="list-style-type: none"> ◊ 0.5% Sodium deoxycholate ◊ 0.1% SDS ◊ 70 mM N-Octyl-beta-D-Glucoside ◊ Protease inhibitor cocktail III (A.G. Scientific) ◊ Phosphatase inhibitor cocktail (Roche) | <ul style="list-style-type: none"> ◊ Protein transfer conditions: ◊ 4-12% gradient gel ◊ Xcell II™ Blot Module ◊ 30 V constant ◊ 1 hour 30 min |
|---|---|---|

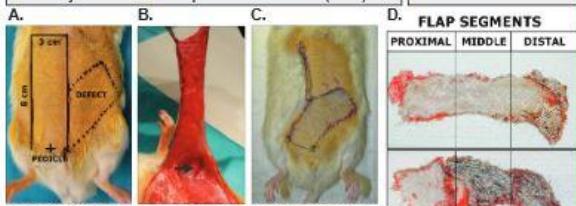
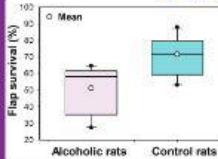


Fig. 1. Pedicled fasciocutaneous flap model. A, Rotational fasciocutaneous flap design. B, Raised pedicled flap. Inferior epigastric artery is shown by black arrow. C, Subject after flap rotation and closure on POD 0. D, Representative photos of relatively viable and necrotic flaps and their segments after harvest on POD 5.

RESULTS: Flap survival



The survival areas of the flaps were clearly demarcated within 5 days time. The surviving skin was pink-white, tender, and normal in its texture. The necrotic skin was black, rigid, dry, and did not bleed when cut. Flap survival was determined as percentage of the non-necrotic flap total flap area in mm² (Fig. 2). Based on planimetric analysis, mean flap survival of rats that were fed alcohol diet was significantly lower than that of control rats - 51.21% \pm 4.59% SEM (standard error) versus 70.16% \pm 3.57% SEM (P = 0.004, t-test assuming equal variances).

Fig. 2. Percentage of flap survival in experimental animal groups. The results are expressed in box plots as mean \pm SD (standard deviation), median (black line), minimal and maximal values (black circles) for each group (n = 3 per group).

RESULTS: Histology and IHC of flaps

Specimens from each segment harvested on POD 5 were put into 10% PBS-buffered formalin, fixed for 24 hours, embedded in paraffin and stained with Masson's Trichrome, H&E or antibodies against endothelial cell marker CD31. The acellular areas were pink and negative for hematoxylin-positive nuclei. Segment necrosis was considered to be full-thickness when involved epidermis, adnexal structures of dermis and subcutaneous adipose tissue (Fig. 3). Inflammatory infiltrate in flaps' fascia contained neutrophils, monocytes and sparse macrophages.

- | | |
|--|---|
| <ul style="list-style-type: none"> GT - granulation tissue; SC - scab; E - epithelium; SF - subcutaneous fat; PC - panniculus carnosus (muscle layer in superficial fascia); D - dermis; | <ul style="list-style-type: none"> KEY colors in Masson's Trichrome (MT) staining: ◊ BRIGHT RED - cytoplasm, muscle, erythrocytes, keratin ◊ DARK PURPLE - cell nuclei; ◊ BLUE - collagen fibers |
|--|---|

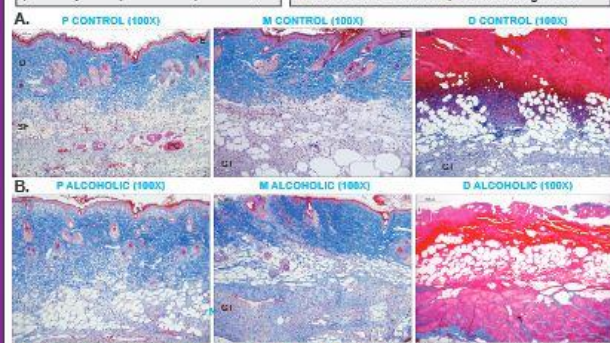


Fig. 3. Low-power photomicrographs of MT stained longitudinal sections of representative proximal (P), middle (M) and distal (D) flap segment specimens from control (A) and alcoholic (B) animal groups. Majority of D segments of control rats showed some degree of cellularity, whereas most alcoholic rat specimens demonstrated full-thickness acellular necrosis.

RESULTS: Protein analysis

First, certain protein markers (see box below) were detected by immunoblotting (IB) in different flap segments to see how their expression reflects the severity of visible necrosis (Fig. 4A). Then the levels of these proteins were compared in control and alcoholic animal pairs separately (Fig. 4B). Finally, an expression of selected proteins in a given flap segment was simultaneously detected in the lysates of every rat pair by using MSWB (Fig. 4C). Protein signal intensities were calculated, normalized and plotted (Figs. 4, 5).

- | | |
|---|--|
| <ul style="list-style-type: none"> ◊ Cleaved (CL) Caspase-3 - apoptosis; ◊ Src family kinases (SFK) [V416] & Hsp27 - wound contraction; ◊ p-ERK1/2 [T202/Y204] - cell proliferation; ◊ p-JNK1 (p46) [T183/Y185] - TNFα-induced cell death [13-14]; ◊ VEGF & FGF-2 - angiogenesis; ◊ MMP-9 (produced by activated neutrophils & macrophages) - ECM, including viable and non viable collagen degradation; marker of chronic wound and inflammation; ◊ α-SMA - marker of vascular smooth muscle cells and of fibroblast differentiation into myofibroblasts; ◊ Collagen type I - deposited by fibroblasts; marker of wound healing. | <ul style="list-style-type: none"> ◊ p-Akt (S473) & p-STAT3 (Y705) - cell survival; ◊ Src family kinases (SFK) [V416] & Hsp27 - wound contraction; ◊ p-PLCγ [S1248] & p-p38 MAPK [T180/Y182] - cell motility; ◊ IL-1β & TNFα - tissue inflammation and death; ◊ CD144 (Vascular endothelial (VE) Cadherin) - vasculature |
|---|--|

RESULTS: Protein analysis

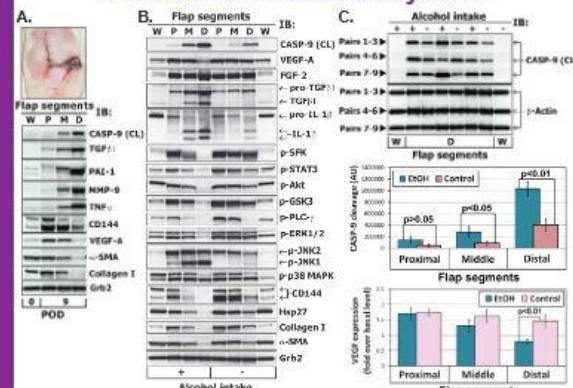


Fig. 4. A, Correlation between the severity of flap failure and the expression of protein markers in healthy (W) skin prior to wounding and proximal (P), middle (M) or distal (D) flap segments at 8th day after raising flap. B, Comparison of protein expression in flap segments of control and alcoholic paired rats. Representative 1 pair with flap survival rates of 73.44% (alcohol intake \rightarrow) and 36.61% (alcohol intake \leftarrow) is shown. W - basal conditions. C, Comparison of protein expression under basal (W) conditions and in distal flap segments of alcoholic and control rats at POD 8. D, VEGF-A levels under basal (W) conditions and in different flap segments of alcoholic and control rats at POD 8.

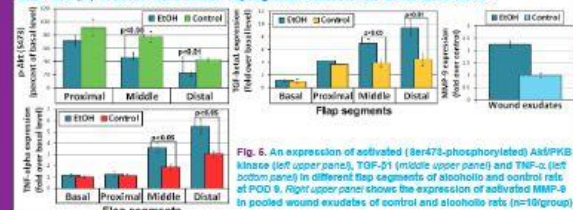


Fig. 6. An expression of activated (Ser473-phosphorylated) Akt/PKB kinase (left upper panel), p-PI3K (middle upper panel) and p-Akt (left bottom panel) in different flap segments of alcoholic and control rats at POD 8. Right upper panel shows the expression of activated MMP-9 in pooled wound exudates of control and alcoholic rats (n=10/group).

CONCLUSION

Chronic alcohol consumption sustains cellular production of pro-inflammatory cytokines, inhibits the anti-apoptotic PI3-kinase/Akt signaling, augments activated MMP-9 levels in wound exudates by 2.25-fold and significantly decreases single-pedicled fasciocutaneous rotational flap survival in aged rats.

ACKNOWLEDGEMENTS

This research was supported by Thomas Jefferson University Department of Otolaryngology - Head & Neck Surgery.

REFERENCES

1. Honrado, DP et al. *Facial Plast Surg Clin N Am* 13 (2005) 200-214
2. Vetter, T et al. *J Int Med Res* 2009; 37: 1502 - 1540
3. Bao, F et al. *J Surg Res* 2009; 151: 193D-197
4. Guo, S & DiPietro, L.A. *J Dent Res* 2010; 89(3): 210-220
5. Ehrlich, SA et al. *Sci Transl Med* 3 (2011) 225-235
6. Han, T et al. *J Biol Chem* 2001; 276: 22341-50
7. Baker, SR. *Local Flaps in Facial Reconstruction*. Elsevier 2007;
8. Sig, S, et al. *Free Radical Research* 2013; 47(11): 994-1004
9. Kwon, J & Akamatsu, T. *Methods Mol Biol* 2009; 520: 149-161
10. Watson, RR. *Alcohol, Drugs of Abuse, and Immune Functions*. In: Akamatsu, E, et al. *Electrophoresis* 2007; 28p 1813-1819.
11. Kwon, J & Akamatsu, T. *Methods Mol Biol* 2009; 520: 149-161
12. Liu, J et al. *Mol Cell Bio* 2004; 24(24): 10844-50
13. Liu, J et al. *PLoS* 1997; 24(20): 13109-13114

PRESENTER: Edita Aksamitiene, PhD
Edita.Aksamitiene@jefferson.edu
THANK YOU for your time!



Epigenetic Mediated Early Induction of Adipocyte Differentiation Contributes to Programmed Obesity in Intrauterine Growth Restricted Newborns

Mina Desai, Ph.D.,¹ Robert H. Lane, M.D.,¹ Guang Han, M.D.,¹ Thomas R. Magee, Ph.D.,¹ and Michael G. Ross, M.D., M.P.H.²
¹Dept. of Obstetrics and Gynecology, Harbor-UCLA Medical Center (LABioMed), Torrance, California; ²Dept. of Neonatology, University of Utah, Salt Lake



ABSTRACT

OBJECTIVE: A key feature of gestationally programmed obesity in intrauterine growth restricted (IUGR) newborns is enhanced adipogenesis. Adipogenesis is driven by adipocyte differentiation, a process whereby previously silent adipogenic genes are activated, in part, via epigenetic mechanisms. DNA methyltransferase (DNMT3a) and histone deacetylase (HDAC1) both suppress gene expression. We have previously shown that maternal food restriction results in IUGR newborns that develop adult obesity. Notably at 1 day of age, IUGR newborns have upregulated expression of adipogenic transcription factors (PPAR γ , C/EBP α). We hypothesized that IUGR adipocytes exhibit enhanced adipocyte differentiation as a result of epigenetic mediated enhanced induction of adipogenic genes. Using primary adipocyte cultures, we determined the degree of induction of epigenetic modulators, adipogenic transcription factors and their downstream lipogenic target genes (SREBP1, fatty acid synthase, acetyl-CoA carboxylase) in IUGR and Control offspring.

METHODS: Control dams received ad libitum food, whereas study dams were 50% food-restricted from pregnancy day 10 to term, resulting in IUGR newborns. Adipose tissue was obtained from 1 day old IUGR and Control newborns and cultured for 48h (time 0), at which time cells were induced to differentiate. Protein was extracted at day 0, 2, 4 and 6 and expression of epigenetic (DNMT3a, HDAC1), adipogenic (PPAR γ , C/EBP α), and lipogenic factors (SREBP1, fatty acid synthase, acetyl-CoA carboxylase) were determined. Values were normalized to GAPDH and presented as fold change.

RESULTS: In IUGR and Control adipocytes, prior to induction at day 0, DNMT3a and HDAC1 were highly expressed, in association with absent expression of adipogenic and lipogenic factors. With induction, IUGR DNMT3a and HDAC1 decreased by 90%, while Control DNMT3a and HDAC1 decreased minimally (30-40%). IUGR demonstrated greater expression of adipogenic (PPAR γ : 2.5 vs 1.8 fold) and lipogenic genes (SREBP1 2.2 vs 1.8 fold), which also occurred earlier in IUGR (peak value at 4 day) as compared to Controls (peak value at 6 day).

CONCLUSION: Enhanced induction of adipogenic genes as a result of highly suppressible DNMT3a and HDAC1 likely contributes to increased adipogenesis and obesity in IUGR offspring.

BACKGROUND & OBJECTIVES

Adipogenesis is induced by pre-adipocyte differentiation and adipocyte proliferation with concomitant induction of adipogenic transcription factor, PPAR γ , followed by activation of lipogenic transcription factor, SREBP1. The activation of previously silent genes is regulated in part by epigenetic mechanisms.

Despite low birth weight, intrauterine growth restricted (IUGR) newborns have a programmed predisposition to adult obesity. Suggesting an enhanced adipogenesis, IUGR newborns have upregulated expression of adipogenic transcription factor (PPAR γ).

DNA methyltransferase (DNMT3a) and histone deacetylase (HDAC1) both suppress gene expression (Figure 1). DNMT3a is responsible for methylation of genes during embryonic development and cell differentiation. HDAC1 deacetylates histones and thus suppresses gene transcription.

We hypothesized that IUGR adipocytes exhibit enhanced adipocyte differentiation as a result of epigenetic mediated enhanced induction of adipogenic genes. Using primary adipocyte cultures, we determined the degree of induction of epigenetic modulators, adipogenic transcription factors and their downstream lipogenic target genes (SREBP1, fatty acid synthase, acetyl-CoA carboxylase) in IUGR and Control offspring.

METHODS

Newborn (p1) Primary Adipocyte Cultures

Study Groups: Control dams received ad libitum food, whereas study dams were 50% food-restricted from pregnancy day 10 to 21 to produce IUGR newborns.

Adipocyte Cultures: Adipose tissue was obtained from 1 day old IUGR and Control newborns and isolated pre-adipocytes were cultured in DMEM media supplemented with 10% FBS and 1% Antibiotic-Antimycotics. At 48h of culture (time 0), cells were induced to differentiate using dexamethasone (1 μ M), methylisobutylxanthine (3.1 mM), and insulin (10 μ g/ml) (Figure 2) and samples collected at 2, 4, and 6 days.

Protein Expression: Protein was extracted from all samples and expression determined (Western Blot) of epigenetic modulators (DNMT3a, HDAC1), adipogenic transcription factor (PPAR γ) and the downstream lipogenic target genes (SREBP1, fatty acid synthase, acetyl-CoA carboxylase). Protein expression was normalized to GAPDH and values are means \pm SE.

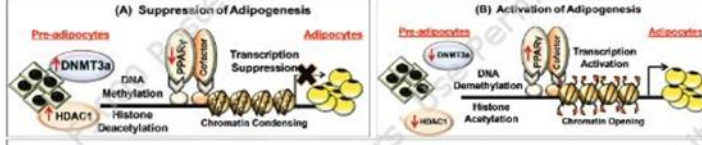


Figure 1. Epigenetic Regulation of Adipocyte Differentiation
 (A) Suppression of Adipogenesis: Increased DNMT3a (methylation) and increased HDAC1 (deacetylation) silences adipogenic gene PPAR γ and hence prevents pre-adipocytes differentiation to adipocytes.
 (B) Activation of Adipogenesis: Decreased DNMT3a (demethylation) and decreased HDAC1 (acetylation) increases transcription of adipogenic gene, PPAR γ and hence induces pre-adipocyte differentiation to adipocytes.

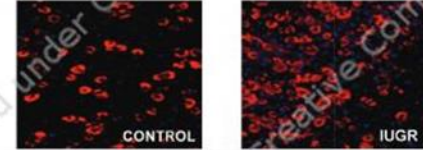


Figure 2. Images of Adipocyte Differentiation
 Control and IUGR pre-adipocytes were cultured in differentiation media over 6 days and stained with Oil-Red (lipid and differentiation marker, red) and DAPI (nuclei, blue). IUGR has markedly increased number of differentiated adipocytes.

RESULTS

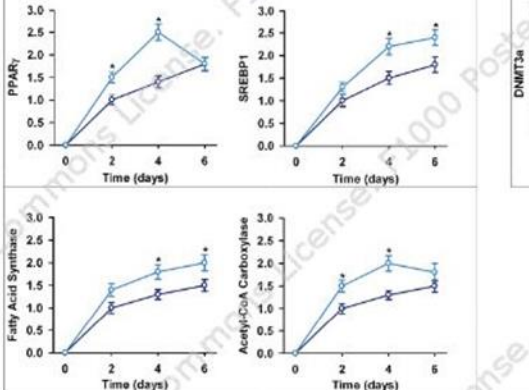


Figure 3. Protein Expression of Transcription and Lipogenic Factors during Adipocyte Differentiation
 Control (solid line) and IUGR (dashed line) pre-adipocytes were cultured in differentiation media over 6 days. Values are mean \pm SE; *P<0.05 vs Control. (1) IUGR adipocytes demonstrated markedly increased adipogenic (PPAR γ) and lipogenic (SREBP1) transcription factors, in association with increased lipid enzymes (fatty acid synthase and acetyl-coA carboxylase) during adipocyte differentiation. (2) Both Control and IUGR pre-adipocytes do not express PPAR γ , SREBP1 and lipid enzymes. (3) IUGR show earlier peak (4 days) as compared to Control (6 days) adipocytes.

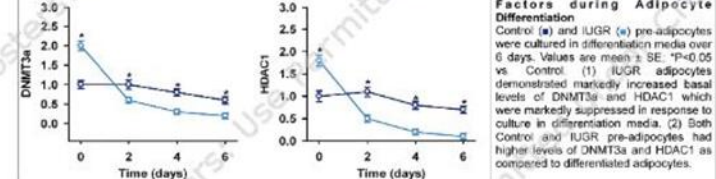


Figure 4. Expression of Epigenetic Factors during Adipocyte Differentiation
 Control (solid line) and IUGR (dashed line) pre-adipocytes were cultured in differentiation media over 6 days. Values are mean \pm SE; *P<0.05 vs Control. (1) IUGR adipocytes demonstrated markedly increased basal levels of DNMT3a and HDAC1 which were markedly suppressed in response to culture in differentiation media. (2) Both Control and IUGR pre-adipocytes had higher levels of DNMT3a and HDAC1 as compared to differentiated adipocytes.

CONCLUSION

- Pre-adipocytes do not express adipose tissue transcription factors or lipogenic enzymes prior to differentiation.
- Increased basal levels of epigenetic factors in IUGR pre-adipocytes suggests a suppression of gene transcription.
- With induction of differentiation, IUGR adipocytes demonstrate a marked reduction of epigenetic silencing factors and an increase in adipogenic transcription factors and lipogenic enzymes.

These results suggest a programmed increased potential for enhanced adipogenesis in IUGR offspring, independent of the body hormonal milieu or offspring diet.

ACKNOWLEDGEMENTS

Grant Funding: M.D. is supported by 5R01DK081756 NIH/NIDDK, and M.G.R. is supported by 5R01HD054751 NIH/NICHD.

INTEGRATE EVERYTHING BUT THE KITCHEN SINK: DATA SET SELECTION AND SENSITIVITY ESTIMATION IN COLLECTIVE FACTOR MODELS

MARINKA ZITNIK¹ & BLAZ ZUPAN^{1,2}

¹UNIVERSITY OF LJUBLJANA, SLOVENIA, ²BAYLOR COLLEGE OF MEDICINE, HOUSTON, USA
MARINKAZITNIK@FRI.uni-lj.si, BLAZ.ZUPAN@FRI.uni-lj.si

WE ACKNOWLEDGE FINANCIAL SUPPORT FROM ARRS, EU FP7 AND THE RESEARCH GROUP 4 BURNED IN ANCONA

JANE & MIKE, PART 3

HEY, JANE! HOW IS YOUR RESEARCH IN DATA FUSION?

INTERESTING! HOW MANY DATA SETS DO YOU USUALLY CONSIDER?

PART 1 PART 2

WE FUSE TENS OF DATA SETS. HERE IS A FUSION SCHEME WITH 18 DATA SETS:

WHO'D YOU FUSED TENS OF DATA SETS? HOW?

WE USUALLY ESTIMATE LATENT DATA REPRESENTATION OF AN ENTIRE DATA COLLECTION.

PROBABLY, WE CAN ESTIMATE SOME OF THE LATENT PATTERNS BETWEEN DATA SETS.

BUT THERE ARE CHALLENGES: HOW DO CHANGES IN ONE DATASET AFFECT THE LATENT SPACE OF ANOTHER DATASET?

FOR EXAMPLE, IN A USER-FOCUS RECOMMENDATION SYSTEM, HOW WOULD A CHANGE OF CATEGORIES AFFECT USER PREFERENCE?

* MITKA & ZUPAN, IEEE SYMBS 2016, 2016, 2016, 2016

CALCULUS 101

ASSUME WE HAVE A SCALAR FUNCTION $f(x)$. CONSIDER NUMBER MEASURES BY HOW MUCH BY MOST SPREAD CHANGES IN THE DATA - CAN BE MEASURED BY THE FUNCTIONAL VALUE BOTH CHANGES ARE MEASURED IN A RELATIVE SENSE.

$$\text{cond}_{rel}(f, x) = \lim_{\Delta x \rightarrow 0} \sup_{\Delta x \in [x, x+\Delta x]} \frac{|f(x+\Delta x) - f(x)|}{\Delta x |f(x)|}$$

HOW WE CAN DEFINE THE NUMBER FOR A MATRIX FUNCTION F : A DATA MATRIX X , AND A PERTURBATION MATRIX E .

$$\text{cond}_{rel}(F, X) = \lim_{\|E\| \rightarrow 0} \sup_{\|E\| \in [X, X+E]} \frac{\|F(X+E) - F(X)\|}{\|F(X)\|}$$

AND I KNOW HOW TO MEASURE SPREAD CHANGES OF THE FUNCTION VALUES. THESE ARE DERIVATIVES:

$$\text{cond}_{rel}(f, x) = \frac{|x^2 f'(x)|}{|f(x)|}$$

APP. BUT WHAT IS THE CORRESPONDING DERIVATIVE OF A MATRIX FUNCTION?

WHEN IT IS JUST A LINEAR OPERATOR THAT SATISFIES THIS CONDITION:

$$F(X+E) - F(X) = L(F, X)E + o(\|E\|)$$

IN OTHER WORDS, IT IS THE FREQUENT DERIVATIVE $F'(X) = L(F, X)$.

UNDERSTANDING MATRIX DERIVATIVES

OH, BUT HOW DOES THIS HELP US BETTER UNDERSTANDING RELATIONSHIPS BETWEEN DATASETS?

IF I SAID YOU RANED LET'S PICK TWO DATASETS FROM OUR FUSION SCHEME, A TARGET DATASET AND AN EFFECT DATASET.

WE USE THE FREQUENT DERIVATIVE TO QUANTIFY THE IMPACT OF CHANGES OF THE EFFECT DATASET ON THE TARGET DATASET.

$$\partial(F^{(T)}, R^{(E)}, F_0) = \frac{\partial C_{F_0}(R^{(T)}, R^{(E)})}{\partial F_0(R^{(E)})} [R^{(T)}]$$

$R^{(T)}$ - TARGET MATRIX
 $R^{(E)}$ - EFFECT MATRIX
 F_0 - COLLECTIVE LEARNING MODEL WITH PARAMETERS θ

LET'S DERIVE THE FORMULA FOR ∂ .

WE KNOW HOW TO ESTIMATE MATRIX NORM OF THE TARGET MATRIX.

AND THE NORM OF THE TARGET RECONSTRUCTION GIVES BY A COLLECTIVE LEARNING MODEL.

WE USE THE FREQUENT DERIVATIVE TO QUANTIFY THE IMPACT OF CHANGES OF THE EFFECT DATASET ON THE TARGET DATASET.

WHAT'S THE MEAN OF THE THIRD PART OF THE FORMULA?

IT IS THE INDUCED MATRIX NORM OF THE FREQUENT DERIVATIVE.

WE CAN WRITE THE FORMULA FOR ∂ :

$$\partial(C_{F_0}(R^{(T)}, R^{(E)}) \| \theta \|) = \frac{\partial C_{F_0}(R^{(T)}, R^{(E)})}{\partial F_0(R^{(E)})} [R^{(T)}]$$

THINK OF IT AS THE BEHAVIOR OF THE TARGET MATRIX WITH RESPECT TO ALL POSSIBLE PERTURBATIONS E .

* MITKA & ZUPAN, IEEE SYMBS 2016

SURE, BUT HOW DO YOU ACTUALLY COMPUTE IT?

IT IS A TRICK IN COMPLEX ARITHMETIC WHICH ALLOWS US TO ESTIMATE IT EXTREMELY EFFICIENTLY.

$$\partial C_{F_0}(R^{(T)}, R^{(E)}; E) \approx \text{Im} \left\{ \frac{F_0(R^{(T)})^\dagger \partial E - \partial E (R^{(T)})^\dagger F_0(R^{(T)})}{2} \right\}$$

WE CAN ESTIMATE SENSITIVITY FOR ALL PAIRS OF DATASETS WITH A SINGLE RUN OF INFERENCE ALGORITHM.

AND WE PROVIDE THEORETICAL GUARANTEES ABOUT ESTIMATION QUALITY.

- $\|R^{(T)}\|$
- $\|F_0(R^{(E)})\|$
- $\|C_{F_0}(R^{(T)}, R^{(E)})\|$

THE ∂ OPERATOR

APP. WHY? WHAT IS THAT USE IN THE FORMULA?

WE INVENTED THE ∂ OPERATOR. IT TRANSFORMS PERTURBATION MATRIX TO THE LATENT SPACE OF THE EFFECT MATRIX.

$$\partial : R^{(E)} \times R^{(E)} \rightarrow R^{(T)} \times R^{(T)}$$

OH, BUT DOES THIS TECHNIQUE WORK ONLY WITH YOUR COLLECTIVE MATRIX FACTORIZATION MODEL F_0 ?

NO, IT IS BEING APPLICABLE TO ANY PRESENT COLLECTIVE LATENT FACTOR MODEL.

IT CAN BE APPLIED TO MULTIPLE, TENSOR OR MULTI-RELATIONAL, MODELS.

Tensor Model: Target relation (matrix), Effect relation (matrix), objects of type E_1 , objects of type E_2 .

Multi-relational and Multiplex Model: Matrix with blocks E_1, E_2, E_3, E_4 and objects O_1, O_2, O_3, O_4 .

* MITKA & ZUPAN, IEEE SYMBS 2016

CASE STUDY #1: 13 DATASETS

HERE IS THE FUSION SCHEME.

EXCLUDING DATA SET WITH THE LARGEST Δ SCORE CONTRIBUTIONS TO THE LARGEST PERTURBATION OF THE TARGET APPROXIMATION.

SPREAD DISTRIBUTIONS HOLD FOR SMALLER EFFECT SIZES.

Model	1st ranked	2nd ranked	8th ranked	9th ranked
DFMF	2.040	2.001	< 0.001	< 0.001
S-NMF	4.179	3.084	< 0.001	< 0.001
HS-SFAP	3.427	3.153	< 0.001	< 0.001
BESCAL	13.832	4.640	0.655	0.637

CASE STUDY #2: DETECTION OF PROBLEMATIC DATASETS IN A COMPENDIUM OF 40 DATASETS

WE EXPERIMENTAL, HOW MANY SENSE ASSOCIATIONS DATASETS.

HERE, WE SEE A SUBSTANTIAL INCREASE OF THE ∂ SCORES FOR TARGET ACCESS ENTIRE DATA COLLECTION.

BEFORE SAMPLE PICKUP OF DATASET

AFTER SAMPLE PICKUP OF DATASET

CASE CLOSED.



EXPERIENCE-DEPENDENT EPIGENOMIC REORGANIZATION



THE UNIVERSITY OF ALABAMA AT BIRMINGHAM
Department of Neurobiology

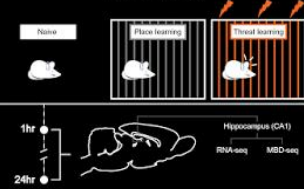
COREY DUKE, ANDREW KENNEDY, CRISTIN GAVIN, DAVID SWEATT, JEREMY DAY

Department of Neurobiology, Evelyn F. McKnight Brain Institute, University of Alabama at Birmingham

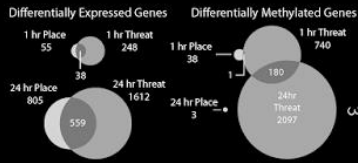
Introduction

The formation and maintenance of new memories requires transcription and translation of genetic material, and epigenetic mechanisms such as methylation and demethylation serve as powerful regulators of gene expression that are crucial to these processes. Moreover, aberrant DNA methylation has been identified in neurological and psychiatric disease states associated with impaired cognition, such as Alzheimer's disease, autism-spectrum disorders, schizophrenia, and drug addiction. Here, we've harnessed whole-genome sequencing tools to systematically characterize memory-related changes in gene expression and DNA methylation status following memory acquisition.

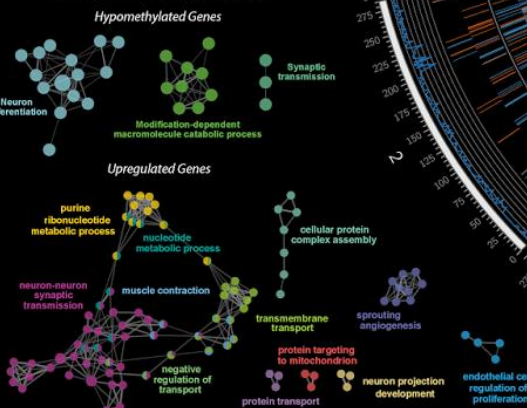
Methods



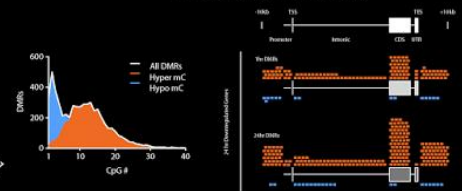
Results



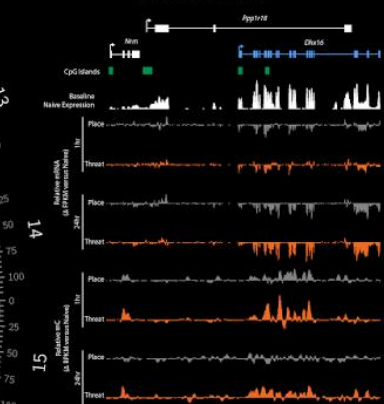
24 hr Threat Learning Gene Ontology



DNA Methylation Site Specificity



Individual Gene Profile



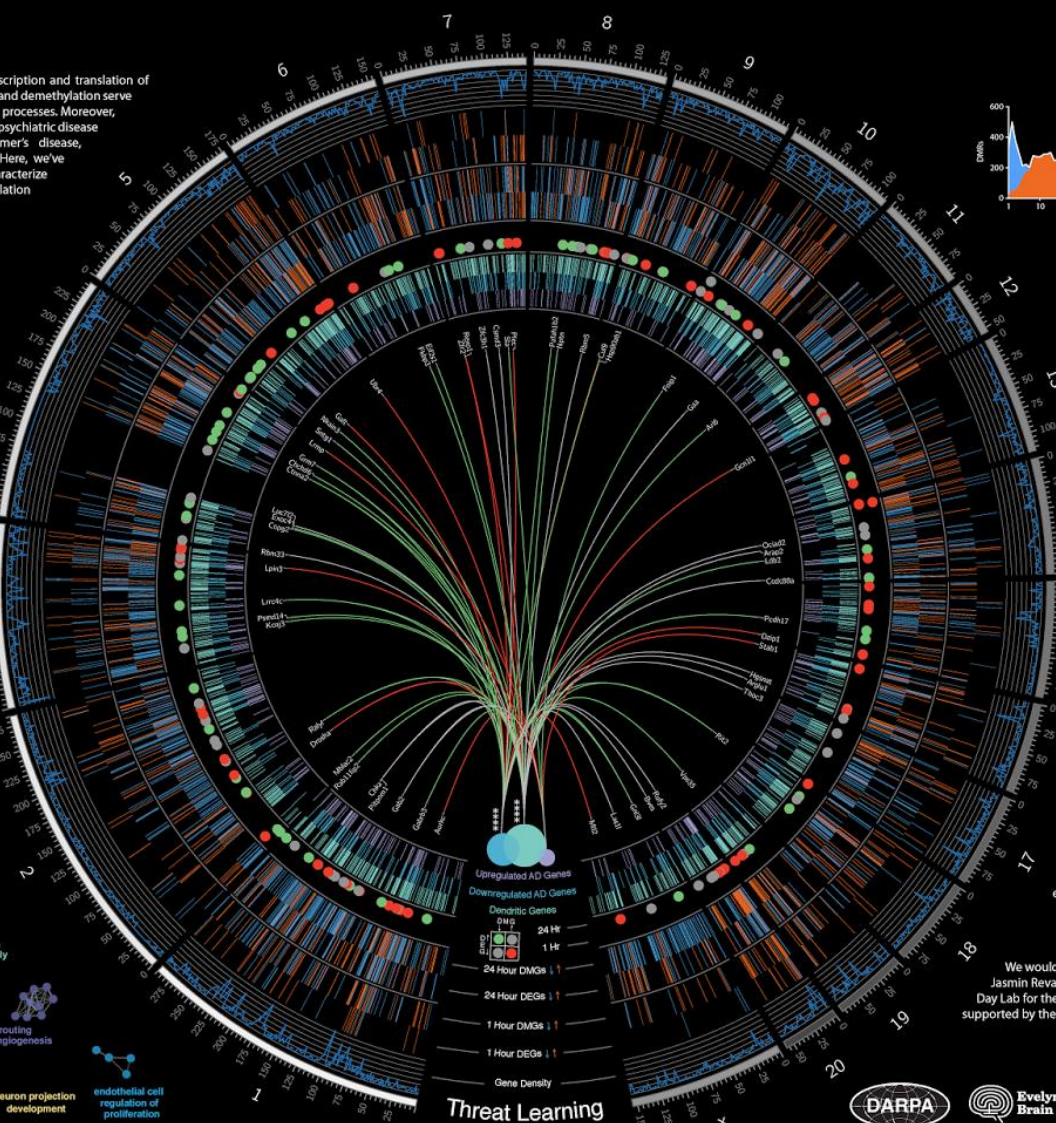
Conclusions/Future Work

Memory acquisition results in thousands of gene expression and epigenomic changes in the rat hippocampus that are experience dependent. These modifications are evident as early as one hour following the learning experience, and become more marked and pronounced after twenty four hours. Several of the coordinately upregulated and downregulated genes following a dramatic learning experience have been implicated in dendritic functions as well as disease states. We hope to further explore the functional significance of these epigenetic marks, and to examine additional time points.

Acknowledgements

We would like to thank Svitlana Bach, Katherine Savell, Rhiana Simon, Jasmin Revanna, Faraz Sultan, Andrew Brane, and the other members of the Day Lab for their helpful discussions and comments. This research was partially supported by the UAB Medical Scientist Training Program.

Funding sources



Jump locations of jump-diffusion with state-dependent rates

Setup

X_t = Markov process with **two (coupled)** noise sources

jump process

characterized by: $\begin{cases} \text{operator } \mathbb{J} \\ \text{rate } \lambda(X_t) \end{cases}$

fixed jump size: $X_{t_+} = X_{t_-} + \Delta$
 $\mathbb{J}q := q(x - \Delta)$

fixed jump location: $X_{t_+} = \eta$
 $\mathbb{J}q := \delta(x - \eta) \int_{-\infty}^{\infty} q(x, t) dx$

diffusion process

characterized by: operator \mathbb{L}
(backward operator)

Itô diffusion: $dY_t = A(Y_t) + \sqrt{2D(Y_t)} dW_t$

$\mathbb{L}q := \partial_y \{A(y)q\} + D(y)\partial_{yy}q$

Chapman-Kolmogorov equation

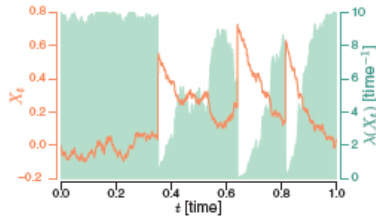
$$\partial_t \tilde{p}(x, t) = \mathbb{L}\tilde{p} - \lambda(x)\tilde{p} + \mathbb{J}\lambda\tilde{p}$$

$\tilde{p}(x, t)$ = density for X_t

Example

$$\mathbb{L}p = \partial_x \{axp\} + Dp_{xx} \quad \lambda = \alpha \exp\{-x^2/\beta\} \quad \mathbb{J}p = p(x - \Delta)$$

$\alpha = -1, D = 1, \alpha = 10, \beta = 10, \Delta = 1$



Jump Locations

$\{t_1, t_2, \dots\}$:= jump times focus of this work
ith jump location := X_{t_i}

other quantities of interest

$\tau_i := t_i - t_{i-1}$:= interjump times

Survival formulation

next jump location $p_j(x) = \int_0^\infty \lambda p dt$

$$\begin{cases} \partial_t p(x, t) = \mathbb{L}p - \lambda p \\ \partial_t q(x, t) = \lambda p \end{cases}$$

next jump time $p_r(t) = \int_{-\infty}^\infty \lambda p dx$

Results

Theorem 1 $p_i(x)$:= distribution of ith jump location, satisfies

$$\begin{cases} \partial_t \hat{p}_i(x, t) = \mathbb{L}\hat{p}_i - \lambda \hat{p}_i \\ \hat{p}_i(x, 0) = \mathbb{J}p_{i-1} \\ p_{i+1}(x) = \int_0^\infty \lambda \hat{p}_i dt \end{cases} \quad (1)$$

more convenient to study $u_i = p_i(x)/\lambda(x)$

Theorem 2 (1) is equivalent to the map

$$\mathbb{T}u_{i+1} = \mathbb{J}u_i \quad \mathbb{T} := [\lambda(x) - \mathbb{L}]$$

importance

can construct sequence $\{u_1, u_2, \dots\}$ and easily recover jump locations $\{p_1, p_2, \dots\}$

Stationarity

Assuming X_t reaches stationarity

p_* := stationary jump distribution, $u_* = p_*/\lambda$

\hat{p}_s := stationary distribution of full process

both satisfy

$$0 = \mathbb{L}u_* - \lambda u_* + \mathbb{J}\lambda u_* \quad 0 = \mathbb{L}\hat{p}_s - \lambda \hat{p}_s + \mathbb{J}\lambda \hat{p}_s$$

explicit connection between jump locations and stationary density

but scaling is different $\int \hat{p}_s dx = 1, \int u_* \lambda dx = 1$

consequence

Theorem 3 stationary distribution $\hat{p}_s = p_*$ jump location distribution iff $\lambda(x) = \lambda_0$ (no state dependence)

Interjump Times

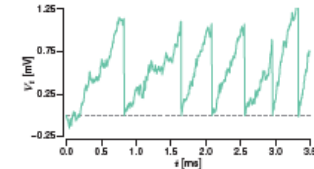
Assuming jump locations $\{p_1, p_2, \dots\}$ known from previous results

Mean interjump time $\langle \tau_i \rangle = \int_{-\infty}^\infty u_i dx$

higher order moments satisfy more complicated (but tractable) differential relationships

Applications

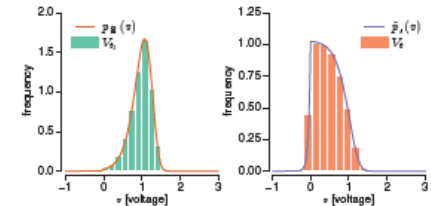
Neuronal Integrate-and-fire



$$\mathbb{L}p = -\partial_v \{avp\} + Dp_{vv}$$

$$\lambda(v) = \gamma e^{v/\beta}$$

$$\mathbb{J}p = \delta(v) \int_{-\infty}^\infty p dv$$

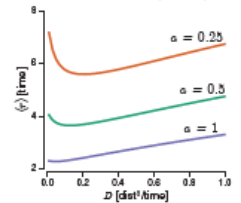
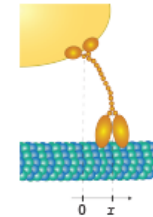


conclusion sharp firing threshold appears as a consequence of stochasticity from state-dependent rate

Molecular Motors?

$$\lambda = \alpha \exp\{-x^2/\beta\}$$

$$\mathbb{L}p = \partial_x \{axp\} + Dp_{xx} \quad \mathbb{J}p = p(x - \Delta)$$



conclusion diffusion may have a non-monotonic effect on motor stepping rate

Future Work

use map formulation to study convergence to stationarity

find more applications (finance?)

relate to state-dependent switched systems (stochastic hybrid systems)

Functional Peptide β -sheets Microsponges

Steven Harris Wibowo, Dr. Adrian Sulistio, Dr. Edgar H. H. Wong, Dr. Anton Blencowe, Prof. Greg G. Qiao*

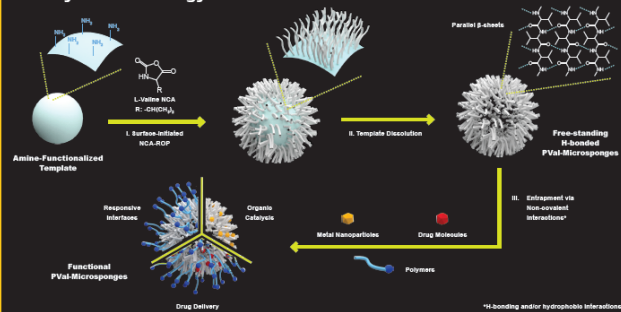
Polymer Science Group, Department of Chemical and Biomolecular Engineering, The University of Melbourne, VIC 3010, Australia
 stevenhw@student.unimelb.edu.au; *gregghq@unimelb.edu.au

1. Introduction

Polypeptides have attracted widespread attention as building block of complex materials due to their ability to form higher-ordered structures such as β -sheets.¹⁻³ Still, the propensity of β -sheet-forming peptides to form irreproducible aggregates in solution remains a critical issue towards the preparation of well-defined β -sheet-assembled materials.

By employing surface-initiated N-carboxyanhydride ring-opening polymerization (SI-ROP), we recently reported a robust strategy to form well-defined peptide β -sheet architectures with sponge-like morphology. Herein, we demonstrate the unique ability of the H-bonded microsponges in entrapping metal nanoparticles, proteins, drug molecules and bio-relevant polymers via non-covalent interactions. This ability mimics the adsorptive ability of marine animals (e.g. sea sponges) and present a simple yet versatile approach towards the fabrication of functional materials for various applications.

2. Synthetic Strategy



3. Results and Discussion

3.1. Synthesis of PVal-microsponges

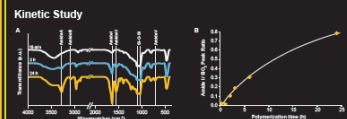


Figure 3.1.1. (A) FTIR spectra of PVal-coated silica particles after various SI-ROP time indicating β -sheets secondary structure. (B) Increase of amine (ν) with polymerization time indicating longer PVal grafts.

Morphology of Hollow PVal-microsponges

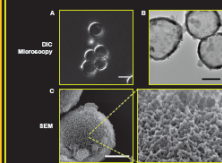


Figure 3.1.2. (A) DIC microscopy and (B) TEM images of hollow PVal-microsponges prepared after 2 h SI-ROP and subsequent template dissolution. (C) SEM images reveal sponge-like morphology. Scale bars: 5 μ m for DIC image and 2 μ m for TEM and SEM.

Size of PVal-microsponges

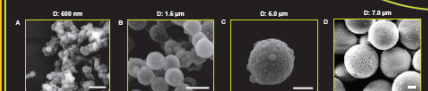


Figure 3.1.3. SEM images reveal PVal-microsponges fabricated by using non-porous silica template with diameter of (A) 500 nm, (B) 1.5 μ m and (C) 5 μ m showing consistent sponge-like morphology. (D) SEM images of PVal-coated mesoporous silica (D: 7 μ m, pore size: 100 nm). Scale bars are 2 μ m.

3.2. Entrapment of Metal

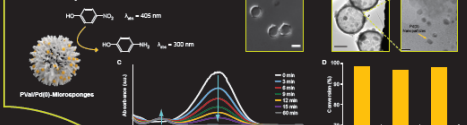


Figure 3.2. (A) UV-Vis spectra of PVal-microsponges before and after AgNO₃ entrapment. (B) TEM images of Ag nanoparticles entrapped in the microsponges (scale bars are 1 μ m, 2 μ m and 10 nm). (C) Evolution of absorbance spectra with increasing hydrogelation reaction time. (D) Conversion achieved in 60 min after 3 catalytic cycles.

3.3. Entrapment of Macromolecules

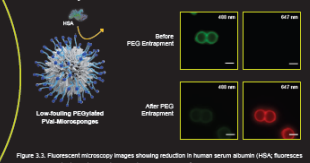


Figure 3.3. Fluorescent microscopy images showing solution in human serum albumin (HSA, fluoresces green) before and after the entrapment of polyethylene glycol (PEG, fluoresces red).

3.4. Multiple macromolecules?

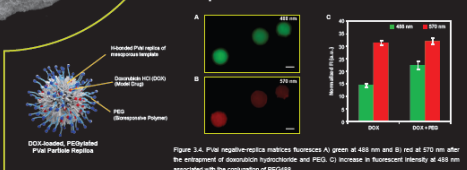


Figure 3.4. PVal negative-charge microsponges fluoresces (A) green at 488 nm and (B) red at 570 nm after the entrapment of bovine serum albumin (HSA) and PEG. (C) Increase in fluorescent intensity of 488 nm associated with the competition of PEG(HSA).

4. Conclusion

The present study demonstrates the facile formation of polypeptide microsponges by employing surface-initiated N-carboxyanhydride ring-opening polymerization. We further demonstrates the ability of the β -sheets-stabilized microsponges in entrapping a range of organic and inorganic materials including metal nanoparticles, proteins, drug molecules and bio-relevant polymers via non-covalent interactions.

Further studies are currently directed at employing this surface-driven approach to fabricate other unique β -sheets-assembled nano/micro-architectures, as well as utilizing the reported hollow PVal-microsponges as platforms for organic catalysis and biomedical devices.

5. References

- H. R. Kricheldorf, *Angew. Chem. Int. Ed.* 2006, 45, 5752-5784
- S. H. Wibowo, A. Sulistio, E. H. H. Wong, A. Blencowe, G. G. Qiao, *Chem. Comm.* 2014, 50, 4971-4988.
- S. L. Goh, A. P. Platt, K. E. Ruffledge, I. Lee, *J. Polym. Sci. A Polym. Chem.* 2008, 46, 5361-5369.

6. Acknowledgement

The authors acknowledge the Australian Research Council under Future Fellowship (FT11010411, G.G.Q.) scheme for financial support of this work. We also thank Dr. Matthew Rowles and Kai Nal for the assistance with XRD and HF treatment, respectively.



Do missing megafauna limit the distributions of some trees?

Benjamin J. Seliger and Jacquelyn L. Gill

Climate Change Institute and School of Biology and Ecology, University of Maine, Orono, ME

The Problem

The mysterious fruits of some trees are best explained when viewed in the megafauna filled world in which they evolved¹ (Fig. 1). Tree species like Joshua Tree, which produce fruit largely uneaten today, were among common foods of now-extinct megaherbivores^{2,3}. Since the Pleistocene megafaunal collapse, trees dependent upon these dispersers should have a reduced ability to track changing climates.



Figure 2: Pleistocene megaherbivores of the American Southwest that could potentially disperse large fruits included ground sloths, proboscideans, Pleistocene camels, and glyptodonts. Illustrations from Encyclopedia Britannica.



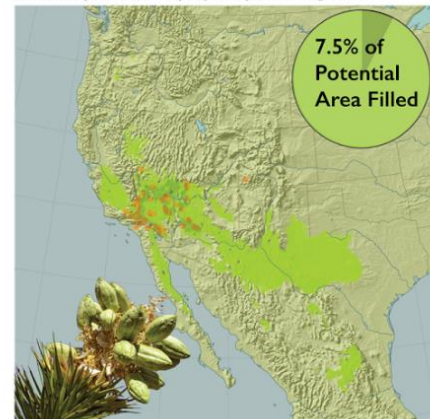
Figure 1: Six North American fruit with adaptations for megafauna dispersal. Megafaunal fruit are often too large to eat or too difficult to open for extant animals, and are sugary or otherwise rich in nutrients. Many are not dispersed today.

We can test this hypothesis using the percentage a species realizes of its bioclimatically potential range as a proxy for dispersal during the Holocene⁴. On this poster, we estimate potential ranges with MaxEnt for Joshua Tree and Honey Mesquite, two species thought to have been dispersed by the community of megaherbivores that lived in the arid American Southwest⁵ (Fig. 2). Results are shown as maps below.

The Data

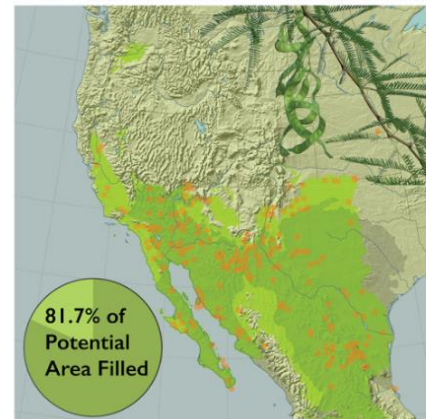
Joshua Tree (*Yucca brevifolia*)

Holocene Dispersers: Secondary dispersal by seed-caching rodents⁶



Honey Mesquite (*Prosopis glandulosa*)

Holocene Dispersers: Deer, coyotes, raccoons, skunks, turkeys and other birds⁷



Joshua Tree and Honey Mesquite differ in the percentage of potential range filled by an order of magnitude. We attributed this difference to the disparity in Holocene dispersers between the two trees. Seed-caching rodents are the only documented dispersers of Joshua Tree today⁶, while several mesofauna species disperse Honey Mesquite⁷. These preliminary data suggest that Joshua Tree's range could be limited due to the loss of megaherbivore dispersers. Future work is going to apply this analysis to suspected megafauna-dispersed species in Eastern North America.

Model Specifications

Method: MaxEnt
Occurrence data: GBIF
Climate Data: WorldClim & CGIAR
Evaluation: 80% training, 20% testing
Threshold: Sum specificity & sensitivity

Model Parameters

Environmental: GDD, avg. winter minimum, water balance, and precipitation seasonality
Realized: Range defined by USGS (E.L. Little)
Potential: Area predicted in atleast 4 out of 5 iterations each with different testing data

Contact info

benjamin.seliger@maine.edu



Literature Cited: 1. Janzen, D. H., & Martin, P. S. 1982. Science.
2. Herrington, M. R. 1933. Southwest museum papers.
3. Lauderer, J. D., & Plunk, P. A. 1934. Carnegie Institution of WA.
4. Sweeney, J. C., & Stone, F. 2004. Ecology Letters.
5. Janzen, D. H. 1986. Annual Review of Ecology and Systematics.
6. Vander Wall, S. B., et al. 2008. Ecoscience.
7. Koeniger, C. L., et al. 2003. Journal of Range Management.
Figure Credits: Fig. 1: public domain images Fig. 2: illustrations
© Encyclopedia Britannica. Maps by Seliger, layers from Natural Earth Data



Bioscience Centre
Secondary Student Training Program

Molecular Dynamics Simulations of Periplasmic Proteins and Peptidoglycan in *Escherichia coli*



University of New South Wales
Faculty of Science, School of Biotechnology

Pranav Lalgudi

Gabriel Velez, Wesley Lay, Nick Fleege, Chengqun Guo, Shuxiang Li, Casey Andrews, Dr. Adrian A. Elcock, Ph.D.

The Periplasm



1. Inner Membrane
2. Periplasm
3. Peptidoglycan
4. Outer Membrane

Figure 1: A diagram showing the layers of the *E. coli* cell wall.

The periplasmic space of *E. coli* is an aqueous space between the two selectively permeable membranes around it. It contains a variety of soluble proteins as well as other sugars and ions. In *E. coli*, it contains a network of peptidoglycan, a mesh of sugars and amino acids, which is thicker in *E. coli* a Gram negative bacterium, than Gram positive bacteria. It takes the pH of the extracellular environment, usually 7.5 or 7.6. The periplasmic space is an important structure that plays a crucial role in protein export, and it can make up a substantial cellular portion, up to 40% of the volume of the cell.

Molecular Dynamics Simulations

Molecular Dynamics (MD) simulations are a powerful tool that can be used to visualize biological molecules and systems. They take coordinates for the atoms in a particular molecule and generate forces acting on them, based on physical and chemical principles and Newtonian dynamics, that act on other atoms within a certain cutoff radius. Below is an example of a commonly used force field:

- $$E_{total} = \sum_i \frac{1}{2} k_b (r_i - r_0)^2 + \sum_{i,j} \frac{1}{2} k_{\theta} (\theta_{ij} - \theta_0)^2 + \sum_{i,j,k} \frac{1}{2} k_{\phi} (\phi_{ijk} - \phi_0)^2 + \sum_{i,j,k,l} \frac{1}{2} k_{\chi} (\chi_{ijkl} - \chi_0)^2 + \sum_{i,j} \frac{q_i q_j}{4\pi\epsilon_0 r_{ij}}$$
1. Bond stretching
 2. Angle bending
 3. Dihedral torsions
 4. Electrostatic
 5. Van der Waals



Figure 2: An MD simulation screenshot of the peptidoglycan layer.

Simulation Information

The simulation was run on a PC computer cluster comprising 21 nodes, with 976 total cores, which possesses the ability to perform massive computations rapidly. The system of the 6 interlinked strands of peptidoglycan was simulated with the top 13 most abundant periplasmic proteins, randomly placed. It was solvated in water, and Na⁺ and Cl⁻ ions were added at a concentration of 150 mM to balance the charge of the system. The AMBER99SBMR1-LDN force field was used, and the TIP4P-Ew water model was used. The production simulation was performed at 25 C.

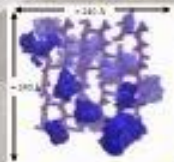


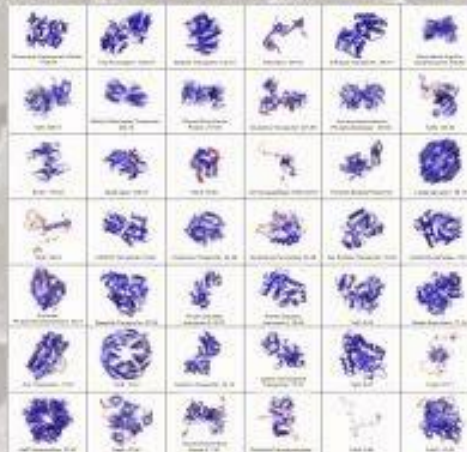
Figure 3: A screenshot of the list of coordinates of the molecules. The proteins used in this simulation: Nucleoside Diphosphate Kinase, Thiol Peroxidase, Malate Transporter, Rotamase, D-Ribose Transporter, Arginine Decarboxylase, TolB, Glucan Biosynthesis Protein, Guanine Transporter, Galactoside Transporter. Protein is shown in blue, and carbohydrates are shown in red.

Methods



Protein Specifics

Structures generated for proteins in the periplasm are shown below with their structures and copy numbers, although only the first 13 are incorporated in the final simulation. Original template regions are shown in blue, while regions added by the modeling program are in red.



Simulation Results

Exploratory 3 ps simulations determined that 6 nodes and 266 cores (96 PME) should be used for optimal performance, yielding respectable ___ ns/day in practice.

Conclusion

In this work, complete model structures for a large number of abundant periplasmic proteins were constructed. A ___ ns long molecular dynamics simulation of the 13 most abundant periplasmic proteins solvated within a box of water and ions, dispersed on either side of a 6 stranded model of the peptidoglycan was run. The interactions between the peptidoglycan layer and the proteins were examined, and ___

Implications

This simulation was another stepping stone on the way to constructing a model of the entire cell. Such a model would prove to be immensely helpful in all areas of the biological sciences, and would advance and revolutionize research, allowing for testing of biological hypotheses in *in silico* systems as well as allowing for verification of *in vivo* results. Future directions and the next steps to perform in the near future are to run simulations with the entire periplasmic protein fraction, and add the inner and outer membranes and proteins, and eventually the cytoplasm, to build a complete, accurate, and comprehensive model of the cellular structure.

Acknowledgements

I am extremely grateful to Dr. Elcock for the invaluable mentorship that he has provided throughout the project, as well as providing me the incredible opportunity to work in his lab, as well as the amazing members of the lab for their guidance. In addition, I would like to sincerely thank Dr. Degroot for her helpful advice and resources throughout this project.

References

1. ...
2. ...
3. ...
4. ...
5. ...

Is the sediment an inexhaustible nutrient supply for benthic microalgae?

Sokratis Papaspyrou^{1,2,a}, Emilio García-Robledo^{1,b}, Julio Bohorquez¹, Juan-Luis Jiménez-Arías¹, Daniel Calenti¹, Alfonso Corzo¹

Email: sokratis.papaspyrou@uca.es

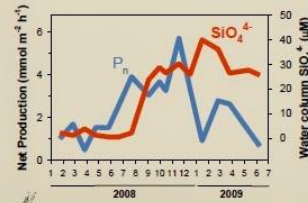
Premise

Benthic microalgae (microphytobenthos, MPB) production is generally considered *not* to be **nutrient limited** due to an inexhaustible supply of nutrients from the sediment.

Net production relates to water column SiO_4^{4-}

Water column nutrients

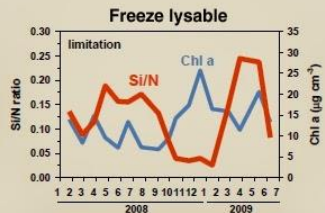
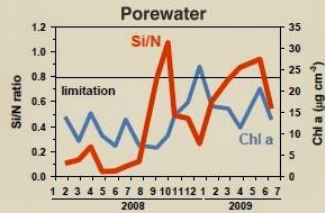
An 18-month study of intertidal muddy sediments from the Bay of Cadiz (SW Spain) showed that MPB net production rates measured with microelectrodes were best explained by the water column silicate supply pattern (18% of variation).



Sediment SiO_4^{4-} is limiting for MPB

Sediment nutrient pools

Analysis of the sediment nutrient pools (0-5mm layer) (i.e. porewater, freeze-lysable and KCl extractable) showed that **silicate** in these pools was **limiting** for MPB diatoms ($\text{Si/N} < 0.79$). In contrast, **no limitation** was found for either the water column or porewater **phosphorus** ($\text{N/P} > 21$).

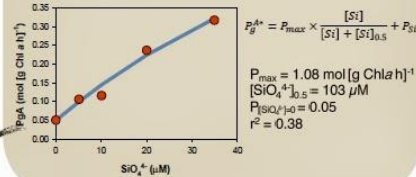


MPB production increases linearly with water column SiO_4^{4-} supply

Laboratory Si enrichment

Amendment of microcosms with silicate (0-35 μM) in laboratory experiments resulted in a linear increase of MPB normalised gross production.

Application of Monod-type semi-saturation curve estimated that $\sim 100 \mu\text{M}$ of silicate would be necessary to saturate MPB demand.



Conclusion

Silicate seems to be a central driving factor for MPB production in Cadiz Bay intertidal sediments
Sediment nutrients may be an important factor limiting MPB production during emersion periods.

Introduction:

Brand perception impacts consumer behavior and even their perception of other people who own items of that brand (Gubb, 1968). This perception is formed not only by a product's physical design, but also through the cognitive processes involved in perceiving the product and any pre-existing assumptions a consumer may have (Leader, 2007). Because brand perception is influenced by multiple factors, it is often difficult to quantify and lacks a significant amount of research. The current body of psychological work on brand perception is lacking in several regards. Previous research indicated that consumer purchasing habits and behavior were motivated by brand alliance in relation to self-perception; however, other research implied that individuals make assumptions about others' self-concepts on the basis of their clothing (Soloman and Rabolt, 1999). Our study aimed to clarify any contradictions and improve the scientific understanding of how SES impacted an individual's perception of a brand that targeted that individual's SES as compared to a brand that did not. To do so, we created a survey in which participants were asked to rate people of varying socioeconomic statuses in terms of personal characteristics followed by questions on brands of various prices to measure positive or negative brand perception.

Discussion:

Overall, out of the eight brands included in the survey, only The North Face produced a statistically significant result. This indicates that among Tufts students, socioeconomic status could influence how items from The North Face are perceived. Those of the middle-to-upper level economic status gave the company an average rating of 5.926, indicating a more positive perception of the brand than those of the lower-to-middle level who evaluated the brand at an average of 5.000. The results from the independent samples t-tests run for the other seven brands did not produce a significant difference in brand perception between higher and lower socioeconomic status. Because the correlation between self-identified SES and brand perception involved a survey to determine participant conditions (self-identified lower-to-middle class or middle-to-upper class) rather than random assignment of condition, this is not a conclusive or causal result as would be in an experiment rather than a survey. Further, according to Gubb, exposure to a brand over time can influence perception (1968), which may have been a confounding factor in our study.



Socioeconomic status does not impact brand perception among university students.

**Method:****Participants**

Forty-six undergraduate students (16 males and 30 females) from Tufts University who chose to answer our demographic questions participated in this experiment. They were either recruited online or through personal connections of the experimenters.

Materials

We utilized Qualtrics Software to create our online survey. They were asked to rate people of a certain socioeconomic status (lower-middle, middle-upper) on four characteristics (intelligent, honest, greedy, and hardworking) on a four point scale (*not very, moderately low, moderately high, and very*) in order to prime the participants to begin thinking about socioeconomic status and their own perceptions. Following these questions, participants were then asked questions regarding their recognition of the interested brands.

Results:

T-test with an Alpha-Rate of 0.05 Examining the Differences Between Brand Perception Across Different Socioeconomic Statuses

Brand/Product	Hypothesized Value	P-Value	Significant Difference?
Swell	Expensive	0.496	No
Nalgene	Inexpensive	0.2947	No
Comme de Garçons	Expensive	0.2469	No
Converse	Inexpensive	0.931	No
Canada Goose	Expensive	0.4788	No
The North Face	Inexpensive	0.00155	Yes
Apple AirPods	Expensive	0.2542	No
Skullcandy	Inexpensive	0.23	No

References:

- Feinberg, R. A., Mann, L., & Jeffrey, Barnright, W. (1992). Clothing and Social Identity. *Clothing and Textiles Research Journal*, 11(1), 18-23. <https://doi.org/10.1177/08927022010100101>
- Gubb, E. L., & Hupp, G. (1968). Perception of Self, Generalized Stereotypes, and Brand Selection. *Journal of Marketing Research*, 5(1), 58. <https://doi.org/10.2307/3149794>
- Levin, H., Carlson, C., & Kneafoss, R. (2007). Product design perception and brand strength. *Thesis*, 24(2), 47. <https://doi.org/10.1007/s003240147>
- Ross, I. (1971). Self-Concept and Brand Preference. *The Journal of Business*, 44(1), 33-60. Retrieved from <http://www.jstor.org/stable/2313434>
- Soloman, M. R., & Rabolt, N. (Eds.). (1999). *Consumer Behavior: In Fashion*. Prentice Hall.
- Young, Jee Han, Joseph C. Nunes, Xavier Deutz (2010) Signaling Status with Luxury Goods: The Role of Brand Prominence. *Journal of Marketing*, July 2010, Vol. 74, No. 4, pp. 15-30. <https://doi.org/10.1509/jmkp.74.4.15>

Poster Resources

Better Posters

<http://betterposters.blogspot.no/>

Ten Simple Rules for a Good Poster Presentation

<https://www.ncbi.nlm.nih.gov/pmc/articles/PMC1876493/>

Designing conference posters

<http://colinpurrington.com/tips/poster-design>

Creating Effective Poster Presentations | An Effective Poster

<https://projects.ncsu.edu/project/posters/>